SIAM J. SCI. COMPUT.
Vol. 47, No. 1, pp. B28–B58

EFFICIENT FULLY DISCRETE FINITE ELEMENT SCHEME FOR THE FERROHYDRODYNAMIC ROSENSWEIG MODEL AND SIMULATIONS OF FERROFLUID ROTATIONAL FLOW PROBLEMS*

GUO-DONG ZHANG†, XIAOMING HE‡, AND XIAOFENG YANG§

Abstract. This article focuses on numerical approximations of the ferrohydrodynamic (FHD) Rosensweig model of ferrofluids, which comprises the Navier–Stokes equations, the angular momentum equations, the magnetization equations, and the magnetostatic equation, as well as the simulations of the ferrofluid rotational flow problems. The model's strong coupling feature, encompassing both linear and nonlinear aspects, poses a significant challenge in the development of efficient numerical algorithms, particularly for fully decoupled-type schemes with unconditional energy stability. A significant new challenge in the Rosensweig model, as opposed to the relatively well-studied Shliomis FHD model, is the coupling with the extra angular momentum equations, particularly seen in the linear coupling between the angular velocity of the particle spinning and the flow velocity, demanding innovative numerical strategies to effectively address this complexity. By introducing a new nonlocal auxiliary variable and constructing an ordinary differential equation with a special structure for it, we can simplify the complex coupling terms in the modified but equivalent governing system via explicit discretization. This novel method, along with the ZEC (zero energy contribution) decoupling method, reconstruction of the magnetostatic equation, the spatial finite element method, and the second-order projection method for hydrodynamics, allows us to obtain a fully discrete scheme that is unconditionally energy stable, fully decoupled, linear, and second-order accurate in time. Only a few independent linear elliptic/parabolic problems with constant coefficients need to be solved at each time step. The unconditional energy stability and well-posedness of the scheme are also established. In addition, simulations, including 2D/3D spin-up and annular flows, are implemented to verify the stability and accuracy of the scheme, with the numerical results exhibiting good agreement with experimental and physical analyses.

Key words. ferrohydrodynamics, finite element, decoupled, second-order, unconditional energy stability, magnetic field

MSC codes. 65N12, 65M12, 65M70

DOI. 10.1137/24M1640914

1. Introduction.

Ferrofluids, colloidal liquids exhibiting robust magnetic properties, can be magnetized when exposed to an external magnetic field but become completely demagnetized in its absence. In response to the application of a magnetic field, ferrofluids can be manipulated or regulated accordingly. These intriguing substances find applications in numerous areas, including magnetic resonance imaging [7],

*Submitted to the journal's Software, High-Performance Computing, and Computational Science and Engineering section February 21, 2024; accepted for publication (in revised form) September 6, 2024; published electronically January 6, 2025.

https://doi.org/10.1137/24M1640914

Funding: The work of the first author was partially supported by National Natural Science Foundation of China (NSFC) grants 12171415 and 12271468. The work of the second author was partially supported by National Science Foundation grant DMS-1818642. The work of the third author was partially supported by National Science Foundation grants DMS-2012490 and DMS-2309731.

†School of Mathematics and Information Sciences, Yantai University, Yantai, 264005, Shandong, People's Republic of China (gdzhang@ytu.edu.cn).

‡Department of Mathematics, Missouri University of Science and Technology, Rolla, MO 65409 USA (hex@mst.edu).

§Corresponding author. Department of Mathematics, University of South Carolina, Columbia, SC 29208 USA (xfyang@math.sc.edu).

loudspeakers [23], magneto-optic sensors [14], hyperthermia therapy for cancer [25], drug delivery [3, 12], waste water treatment [31], vibration control [44], and in other engineering operations [15]. Two well-known mathematical FHD models, attributed to their respective developers, are the Shliomis model [33, 34], treating particle spin as a magnetic moment, and the Rosensweig model [26, 27], which formulates the angular momentum equation for angular velocity to compute spin.

We recall that some theoretical results, such as well-posedness, regularity, and long time behavior for the FHD models, were studied in [1, 2, 22, 30, 37, 39]. Nonetheless, the design and analysis of numerical algorithms for Rosensweig-type FHD models are still in their early stages of development, particularly due to the inherent complexity arising from the strong coupling nature of the angular momentum equation with others, whereas numerical work on the Shliomis model has been conducted to a greater extent. For instance, in [20], the simplified Shliomis FHD model was combined with the phase-field method to generate a two-phase FHD system, and an unconditionally energy stable scheme, yet nonlinear and coupled, was proposed and analyzed. In [40], for the Shliomis FHD model, a nonlinear and coupled scheme was proposed, and its corresponding error estimates are also derived. In [45], for the two-phase Shliomis FHD model, a linear, partially decoupled, and unconditionally energy stable scheme was developed. Note that the algorithms proposed in the above works exhibit first-order accuracy in terms of time. The recent study [47] improved the temporal order by proposing a second-order accurate, fully decoupled, linear, and unconditionally energy stable scheme for the two-phase Shliomis FHD system. Regarding numerical algorithms for the Rosensweig model, to the best of the authors' knowledge only a nonlinear, coupled, first-order accurate, and unconditionally energy-stable scheme has been proposed in [21], and simulations are limited to the 2D case.

Therefore, the aim of this paper is to propose an efficient scheme for the Rosensweig FHD model, characterized by linearity, full decoupling, second-order accuracy in time, and unconditional energy stability, and to carry out simulations of 2D and 3D ferrofluid rotational flow problems. As previously stated, the limited amount of numerical methods tailored for the Rosensweig model can be attributed to the intricate nature of the angular momentum equation and the diverse couplings it entails. In contrast to the Shliomis model, the Rosensweig model incorporates two kinds of couplings, including the nonlinear type (between the magnetization and magnetic potential, the fluid velocity and the angular velocity, the fluid velocity and magnetization, and angular velocity and magnetization) and the linear type (between the fluid velocity and the angular velocity of particles, the magnetization and magnetic potential, and the fluid velocity and the pressure). The presence of these couplings pose a significant obstacle in the development of efficient algorithms.

Here we provide a concise overview of our methodology for achieving decoupling in different forms of couplings. Regarding the nonlinear coupling terms, it's worth noting that they display a property referred to as zero energy contribution (ZEC), which emerges during the derivation of energy law for the system of partial differential equations (PDEs). More specifically, each PDE undergoes an inner product operation with one or more designated variables, and the resulting inner products involving these nonlinear terms ultimately combine in a manner that leads to mutual cancellation or equating to zero. A highly efficient decoupling technique, known as the ZEC decoupling method [41, 42, 43], has recently been developed. This approach allows for the explicit discretization of nonlinear coupling terms with the ZEC property and yields a decoupled scheme that satisfies energy stability.

There are two categories that pose challenges in terms of discretization. One is the linear coupling terms associated with fluid velocity and angular velocity, resulting in the emergence of a squared diffusion term in the energy law. The other is the linear coupling terms involving the magnetic potential and the magnetization field. To attain the schemes we aim for, we address these two distinct linear couplings in distinct manners.

- For the linear couplings associated with fluid velocity and angular velocity, we introduce an auxiliary variable and define its associated ODE, which comprises the cross terms within the square-type diffusivity terms. The ODE, with its distinctive form, maintains a continuous solution that remains constant at 1. This attribute can be utilized to modify the cross-multiplication term within the constituent square terms of the original system in an equivalent fashion, thereby enabling explicit discretization. Subsequently, the energy inequality can be derived by leveraging the unique structure of this ODE and employing techniques such as Cauchy–Schwarz and Hölder inequalities.
- For the linear coupling terms concerning the magnetic potential and magnetization field, we effect a transformation of the static magnetic equations into dynamic equations with time derivatives by amalgamating these two equations. This transformation results in the elimination of the linear coupling terms, albeit introducing certain nonlinear coupling terms. Intriguingly, these newly generated nonlinear coupling terms exhibit compliance with the ZEC property. Consequently, we can effectively employ the ZEC decoupling method for processing, which ultimately allows us to achieve the desired decoupled scheme.

By integrating the aforementioned numerical techniques and incorporating the projection method to address the linear coupling between fluid velocity and pressure, we successfully arrive at a linear, fully decoupled, second-order time-accurate, and unconditionally energy stable scheme for the Rosensweig FHD model. Our proposed algorithm decomposes the nonlinearly coupled saddle-point structural model into independent linear elliptic/parabolic problems with constant coefficients, facilitating efficient solutions using fast solvers. We also rigorously prove the energy stability and the unique solvability followed by our proposed scheme and verify the accuracy and stability by several numerical examples.

Having established our numerical scheme, we extend its application to conduct simulations reflecting practical scenarios involving ferrofluids. One unique feature of the ferrofluid is that it can be magnetized in applied magnetic fields, which stimulates many control-based applications. Among them, the induced motion of ferrofluid flow by external rotational magnetic fields stands as a significant nonmechanically driven phenomenon, attracting considerable attention in the field of fluid physics [5, 6, 8, 16, 24, 28, 35]. A further contribution of this work is the application of the Rosensweig model and our proposed scheme to simulate two ferrofluid rotational flow problems, the 2D/3D spin-up and annulus flows. The numerical outcomes closely align with results from both experimental and theoretical analyses. Our simulations provide valuable investigations of ferrofluid rotational flow problems, complementing the predominantly experimental studies and physical explanations with additional numerical insights.

We organize the remainder of this article as follows. In section 2, we introduce the Rosensweig FHD model and demonstrate its energy stability. Section 3 outlines the reformulation of the Rosensweig model using various numerical techniques to render it into a more algorithm-friendly form. Section 4 presents the fully discrete finite element numerical scheme and establishes its unconditional stability and well-posedness. In

section 5, we conduct a series of 2D/3D numerical simulations. Finally, section 6 offers concluding remarks.

2. Rosensweig FHD model. Let $\Omega \subset \mathbb{R}^d$ with $d = 2$ or 3 be a simply connected, bounded domain. The Rosensweig model for a viscous, homogenous, incompressible ferrofluid flow system reads as follows [26, 27]:

$$\boldsymbol{u}_t - (\nu + \nu_r)\Delta \boldsymbol{u} + (\boldsymbol{u}\cdot\nabla)\boldsymbol{u} + \nabla p = 2\nu_r \nabla\times \boldsymbol{w} + \mu(\boldsymbol{m}\cdot\nabla)\boldsymbol{h}, \tag{2.1}$$

$$\nabla\cdot\boldsymbol{u} = 0, \tag{2.2}$$

$$\zeta \boldsymbol{w}_t + \zeta(\boldsymbol{u}\cdot\nabla)\boldsymbol{w} - c_1\Delta\boldsymbol{w} - c_2\nabla\nabla\cdot\boldsymbol{w} + 4\nu_r\boldsymbol{w} = 2\nu_r\nabla\times\boldsymbol{u} + \mu\boldsymbol{m}\times\boldsymbol{h}, \tag{2.3}$$

$$\boldsymbol{m}_t + (\boldsymbol{u}\cdot\nabla)\boldsymbol{m} = \boldsymbol{w}\times\boldsymbol{m} - \frac{1}{\tau}(\boldsymbol{m} - \chi_0\boldsymbol{h}), \tag{2.4}$$

$$-\Delta\varphi = \nabla\cdot(\boldsymbol{m} - \boldsymbol{h}_a), \tag{2.5}$$

$$\boldsymbol{u}|_{\partial\Omega} = \boldsymbol{0}, \quad \boldsymbol{w}|_{\partial\Omega} = \boldsymbol{0}, \quad \partial_n\varphi|_{\partial\Omega} = (\boldsymbol{h}_a - \boldsymbol{m})\cdot\boldsymbol{n}_{\partial\Omega}, \tag{2.6}$$

$$\boldsymbol{u}|_{t=0} = \boldsymbol{u}_0, \quad \boldsymbol{w}|_{t=0} = \boldsymbol{w}_0, \quad \boldsymbol{m}|_{t=0} = \boldsymbol{m}_0, \tag{2.7}$$

where (2.1)–(2.2) represent the incompressible hydrodynamical system; $\boldsymbol{u}$ is the fluid velocity; p is the pressure; (2.3) is the angular momentum equation; $\boldsymbol{w}$ is the angular velocity; (2.4) corresponds to the magnetization equation; $\boldsymbol{m}$ is the magnetization field; $\boldsymbol{h}(:= \nabla\varphi)$ is the effective magnetic field; (2.5) is the magnetostatic equation; φ is the magnetic potential; $\boldsymbol{h}_a$ is a smooth harmonic applied magnetic field with the properties of $\nabla\times\boldsymbol{h}_a = \boldsymbol{0}$ and $\nabla\cdot\boldsymbol{h}_a = 0$; ν, ν_r, c_1, and c_2 are the kinematic viscosities; ζ is the inertia density; χ_0 is magnetic susceptibility; μ is permeability of free space; τ is relaxation time constant; $\boldsymbol{n}_{\partial\Omega}$ is the outward normal on the boundary $\partial\Omega$; and the term $(\boldsymbol{m}\cdot\nabla)\boldsymbol{h}$ is the so-called Kelvin force.

Remark 2.1. For the 2D case, $\boldsymbol{x} = (x, y) \in \Omega$, $\boldsymbol{w} = (0, 0, w(x, y))$, hence $\nabla\cdot\boldsymbol{w} = \frac{\partial 0}{\partial x} + \frac{\partial 0}{\partial y} + \frac{\partial w(x,y)}{\partial z} = 0$, and the angular momentum equation (2.3) degenerates to

$$\zeta w_t + \zeta(\boldsymbol{u}\cdot\nabla)w - c_1\Delta w + 4\nu_r w = 2\nu_r\nabla\times\boldsymbol{u} + \mu\boldsymbol{m}\times\boldsymbol{h}.$$

Hereafter, we denote $\boldsymbol{h}_b = (\boldsymbol{h}_a)_t$. For two vector functions $\boldsymbol{u}$, $\boldsymbol{v}$, we denote the L^2 inner product as $(\boldsymbol{u}, \boldsymbol{v}) = \int_\Omega \boldsymbol{u}\cdot\boldsymbol{v}d\boldsymbol{x}$ and the L^2 norm as $\|\boldsymbol{u}\| = \sqrt{(\boldsymbol{u}, \boldsymbol{u})}$. We use $H^1(\Omega)$ to denote the usual Sobolev space and define $H_0^1(\Omega) = \{\omega \in H^1(\Omega) : \omega|_{\partial\Omega} = 0\}$, $L_0^2(\Omega) = \{\omega \in L^2(\Omega) : \int_\Omega \omega dx = 0\}$, $\boldsymbol{H}^1(\Omega) = H^1(\Omega)^d$, and $\boldsymbol{H}_0^1(\Omega) = H_0^1(\Omega)^d$.

The Rosensweig FHD model (2.1)–(2.7) satisfies the following energy stability and dissipative law.

THEOREM 2.1. *The system* (2.1)–(2.7) *admits the energy stability as*

$$\frac{d}{dt}E(\boldsymbol{u}, \boldsymbol{w}, \boldsymbol{h}, \boldsymbol{m}) + D(\boldsymbol{u}, \boldsymbol{w}, \boldsymbol{h}, \boldsymbol{m}) \le \frac{\mu}{\tau}\|\boldsymbol{h}_a\|^2 + \tau\mu\|\boldsymbol{h}_b\|^2. \tag{2.8}$$

If the applied magnetic field is absent ($\boldsymbol{h}_a = \boldsymbol{0}$)*, the system holds the energy dissipative law as*

$$\frac{d}{dt}E(\boldsymbol{u}, \boldsymbol{w}, \boldsymbol{h}, \boldsymbol{m}) + D(\boldsymbol{u}, \boldsymbol{w}, \boldsymbol{h}, \boldsymbol{m}) \le 0, \tag{2.9}$$

where

$$\begin{aligned} E(\boldsymbol{u}, \boldsymbol{w}, \boldsymbol{h}, \boldsymbol{m}) &= \frac{1}{2}\|\boldsymbol{u}\|^2 + \frac{\zeta}{2}\|\boldsymbol{w}\|^2 + \frac{\mu}{2}\|\boldsymbol{h}\|^2 + \frac{\mu}{2\chi_0}\|\boldsymbol{m}\|^2, \\ D(\boldsymbol{u}, \boldsymbol{w}, \boldsymbol{h}, \boldsymbol{m}) &= \nu\|\nabla\boldsymbol{u}\|^2 + \nu_r\|\nabla\cdot\boldsymbol{u}\|^2 + \nu_r\|\nabla\times\boldsymbol{u} - 2\boldsymbol{w}\|^2 + c_1\|\nabla\boldsymbol{w}\|^2 \\ &\quad + c_2\|\nabla\cdot\boldsymbol{w}\|^2 + \frac{\mu}{2\tau}\|\boldsymbol{h}\|^2 + \frac{3\mu}{4\tau\chi_0}\|\boldsymbol{m}\|^2. \end{aligned}$$

Proof. Taking the L^2 inner product of (2.1) with $\boldsymbol{u}$ and integration by parts, we derive

$$\begin{aligned}(2.10)\qquad &\frac{1}{2}\frac{d}{dt}\|\boldsymbol{u}\|^2+\nu\|\nabla\boldsymbol{u}\|^2+\nu_r\|\nabla\times\boldsymbol{u}\|^2+\nu_r\|\nabla\cdot\boldsymbol{u}\|^2\\&\quad=-((\boldsymbol{u}\cdot\nabla)\boldsymbol{u},\boldsymbol{u})+2\nu_r(\boldsymbol{w},\nabla\times\boldsymbol{u})+\mu((\boldsymbol{m}\cdot\nabla)\boldsymbol{h},\boldsymbol{u}),\end{aligned}$$

where we apply the identity of $-\nu_r\Delta\boldsymbol{u}=\nu_r\nabla\times\nabla\times\boldsymbol{u}-\nu_r\nabla\nabla\cdot\boldsymbol{u}$. Taking the L^2 inner product of (2.3) with $\boldsymbol{w}$ and using integration by parts, we get

$$\begin{aligned}(2.11)\qquad &\frac{\zeta}{2}\frac{d}{dt}\|\boldsymbol{w}\|^2+\zeta((\boldsymbol{u}\cdot\nabla)\boldsymbol{w},\boldsymbol{w})+c_1\|\nabla\boldsymbol{w}\|^2+c_2\|\nabla\cdot\boldsymbol{w}\|^2+4\nu_r\|\boldsymbol{w}\|^2\\&\quad=2\nu_r(\nabla\times\boldsymbol{u},\boldsymbol{w})+\mu(\boldsymbol{m}\times\boldsymbol{h},\boldsymbol{w}).\end{aligned}$$

Taking the L^2 inner product of (2.4) with $-\mu\boldsymbol{h}$, we derive

$$\begin{aligned}(2.12)\qquad &-\mu(\boldsymbol{m}_t,\boldsymbol{h})+\frac{\mu}{\tau}\chi_0\|\boldsymbol{h}\|^2\\&=\mu((\boldsymbol{u}\cdot\nabla)\boldsymbol{m},\boldsymbol{h})-\mu(\boldsymbol{w}\times\boldsymbol{m},\boldsymbol{h})+\frac{\mu}{\tau}(\boldsymbol{m},\boldsymbol{h}).\end{aligned}$$

Taking the L^2 inner product of (2.5) with $\frac{\mu}{\tau}\varphi$, using integration by parts, and noting that $\boldsymbol{h}=\nabla\varphi$, we derive

$$(2.13)\qquad \frac{\mu}{\tau}\|\boldsymbol{h}\|^2+\frac{\mu}{\tau}(\boldsymbol{m},\boldsymbol{h})=\frac{\mu}{\tau}(\boldsymbol{h}_a,\boldsymbol{h}).$$

Taking the time derivative of (2.5), we obtain

$$(2.14)\qquad -\Delta\varphi_t=\nabla\cdot(\boldsymbol{m}_t-\boldsymbol{h}_b).$$

Then, taking the L^2 inner product of (2.14) with $\mu\varphi$ and using integration by parts and $\boldsymbol{h}=\nabla\varphi$, we get

$$(2.15)\qquad \frac{\mu}{2}\frac{d}{dt}\|\boldsymbol{h}\|^2+\mu(\boldsymbol{m}_t,\boldsymbol{h})=\mu(\boldsymbol{h}_b,\boldsymbol{h}).$$

Taking the L^2 inner product of (2.4) with $\frac{\mu}{\chi_0}\boldsymbol{m}$, we derive

$$(2.16)\qquad \frac{\mu}{2\chi_0}\frac{d}{dt}\|\boldsymbol{m}\|^2+\frac{\mu}{\chi_0}((\boldsymbol{u}\cdot\nabla)\boldsymbol{m},\boldsymbol{m})+\frac{\mu}{\tau\chi_0}\|\boldsymbol{m}\|^2=\frac{\mu}{\chi_0}(\boldsymbol{w}\times\boldsymbol{m},\boldsymbol{m})+\frac{\mu}{\tau}(\boldsymbol{h},\boldsymbol{m}).$$

Summing up (2.10)–(2.13) and (2.15)–(2.16), we derive

$$\begin{aligned}(2.17)\qquad &\frac{1}{2}\frac{d}{dt}\|\boldsymbol{u}\|^2+\frac{\zeta}{2}\frac{d}{dt}\|\boldsymbol{w}\|^2+\frac{\mu}{2}\frac{d}{dt}\|\boldsymbol{h}\|^2+\frac{\mu}{2\chi_0}\frac{d}{dt}\|\boldsymbol{m}\|^2+\nu\|\nabla\boldsymbol{u}\|^2+\nu_r\|\nabla\cdot\boldsymbol{u}\|^2+c_1\|\nabla\boldsymbol{w}\|^2\\&\quad+c_2\|\nabla\cdot\boldsymbol{w}\|^2+\frac{\mu}{\tau}\chi_0\|\boldsymbol{h}\|^2+\frac{\mu}{\tau}\|\boldsymbol{h}\|^2+\frac{\mu}{\tau\chi_0}\|\boldsymbol{m}\|^2+\nu_r\|\nabla\times\boldsymbol{u}-2\boldsymbol{w}\|^2\\&=\frac{\mu}{\tau}(\boldsymbol{h}_a,\boldsymbol{h})+\mu(\boldsymbol{h}_b,\boldsymbol{h})+\frac{\mu}{\tau}(\boldsymbol{h},\boldsymbol{m}),\end{aligned}$$

where we note a combination of several terms that will eventually form a perfect square that reads as follows:

$$(2.18)\qquad \nu_r\|\nabla\times\boldsymbol{u}\|^2-4\nu_r(\boldsymbol{w},\nabla\times\boldsymbol{u})+4\nu_r\|\boldsymbol{w}\|^2=\nu_r\|\nabla\times\boldsymbol{u}-2\boldsymbol{w}\|^2,$$

and employ several identities that either mutually cancel one another or are inherently zero, expressed as follows:

(2.19)
$$((\boldsymbol{u}\cdot\nabla)\boldsymbol{u},\boldsymbol{u})=0,\ \frac{\mu}{\chi_0}((\boldsymbol{u}\cdot\nabla)\boldsymbol{m},\boldsymbol{m})=0,\ \zeta((\boldsymbol{u}\cdot\nabla)\boldsymbol{w},\boldsymbol{w})=0,\ \frac{\mu}{\chi_0}(\boldsymbol{w}\times\boldsymbol{m},\boldsymbol{m})=0,$$

(2.20)
$$\mu(\boldsymbol{m}\times\boldsymbol{h},\boldsymbol{w})-\mu(\boldsymbol{w}\times\boldsymbol{m},\boldsymbol{h})=0,$$

(2.21)
$$\mu((\boldsymbol{m}\cdot\nabla)\boldsymbol{h},\boldsymbol{u})+\mu((\boldsymbol{u}\cdot\nabla)\boldsymbol{m},\boldsymbol{h})=\mu((\boldsymbol{u}\cdot\nabla)\boldsymbol{h},\boldsymbol{m})+\mu((\boldsymbol{u}\cdot\nabla)\boldsymbol{m},\boldsymbol{h})=0,$$

where we have used integration by parts and $\nabla\times\boldsymbol{h}=\nabla\times\nabla\varphi=\boldsymbol{0}$, $\nabla\cdot\boldsymbol{u}=0$, $\boldsymbol{u}|_{\partial\Omega}=\boldsymbol{0}$.

In addition, by using the Cauchy–Schwarz inequality, we derive

(2.22)
$$\begin{aligned}&\frac{\mu}{\tau}(\boldsymbol{h}_a,\boldsymbol{h})+\mu(\boldsymbol{h}_b,\boldsymbol{h})\\&\quad\le\frac{\mu}{\tau}\|\boldsymbol{h}_a\|\|\boldsymbol{h}\|+\mu\|\boldsymbol{h}_b\|\|\boldsymbol{h}\|\le\frac{\mu}{4\tau}\|\boldsymbol{h}\|^2+\frac{\mu}{\tau}\|\boldsymbol{h}_a\|^2+\frac{\mu}{4\tau}\|\boldsymbol{h}\|^2+\tau\mu\|\boldsymbol{h}_b\|^2,\end{aligned}$$

(2.23)
$$\frac{\mu}{\tau}(\boldsymbol{h},\boldsymbol{m})\le\frac{\mu}{\tau}\|\boldsymbol{h}\|\|\boldsymbol{m}\|\le\frac{\mu}{4\tau\chi_0}\|\boldsymbol{m}\|^2+\frac{\chi_0\mu}{\tau}\|\boldsymbol{h}\|^2.$$

Thus, by combining (2.17) with (2.22)–(2.23), we have

$$\begin{aligned}&\frac{1}{2}\frac{d}{dt}\|\boldsymbol{u}\|^2+\frac{\zeta}{2}\frac{d}{dt}\|\boldsymbol{w}\|^2+\frac{\mu}{2}\frac{d}{dt}\|\boldsymbol{h}\|^2+\frac{\mu}{2\chi_0}\frac{d}{dt}\|\boldsymbol{m}\|^2+\nu\|\nabla\boldsymbol{u}\|^2+\nu_r\|\nabla\cdot\boldsymbol{u}\|^2\\&\quad+c_1\|\nabla\boldsymbol{w}\|^2+c_2\|\nabla\cdot\boldsymbol{w}\|^2+\frac{\mu}{2\tau}\|\boldsymbol{h}\|^2+\frac{3\mu}{4\tau\chi_0}\|\boldsymbol{m}\|^2+\nu_r\|\nabla\times\boldsymbol{u}-2\boldsymbol{w}\|^2\\&\le\frac{\mu}{\tau}\|\boldsymbol{h}_a\|^2+\tau\mu\|\boldsymbol{h}_b\|^2,\end{aligned}$$

which implies (2.8) and (2.9). ∎

Remark 2.2. In the target Rosensweig FHD system (2.1)–(2.7), there exist three pairs of linear couplings: $\boldsymbol{u}$-p, $\boldsymbol{u}$-$\boldsymbol{w}$, and $\boldsymbol{m}$-φ. Among these, the $\boldsymbol{u}$-$\boldsymbol{w}$ coupling, introduced through the angular momentum equation, presents a novel numerical challenge in designing a decoupled scheme compared to the Shliomis FHD model. Additionally, the Rosensweig FHD system (2.1)–(2.7) comprises numerous coupled and nonlinear terms involving the variables $\boldsymbol{u}$, $\boldsymbol{w}$, $\boldsymbol{m}$, and φ. Consequently, to efficiently discretize these terms while achieving energy stability, linearity, and decoupling, we reconfigure the original PDE system into a more algorithm-friendly and equivalent version in the following section.

3. Equivalent reformulation for couplings.

3.1. Linear couplings $\boldsymbol{u}$-p, $\boldsymbol{u}$-$\boldsymbol{w}$, and $\boldsymbol{m}$-φ.

Given that it is widely recognized that the second-order pressure projection method [11, 32] can effectively handle the linear coupling $\boldsymbol{u}$-p to obtain the decoupled type computations between $\boldsymbol{u}$ and p, we mainly focus on the more intricate linear couplings $\boldsymbol{u}$-$\boldsymbol{w}$ and $\boldsymbol{m}$-φ in this subsection.

3.1.1. $\boldsymbol{u}$-$\boldsymbol{w}$ linear coupling.

Here, we address the linear coupling between $\boldsymbol{u}$ and $\boldsymbol{w}$ in (2.1)–(2.3). To simplify the complexity, we focus solely on the related terms of $\boldsymbol{u}$-$\boldsymbol{w}$ linear coupling, and the other terms within (2.1)–(2.3) are denoted as "$\cdots$", namely,

$$\boldsymbol{u}_t + \nu_r \nabla \times \nabla \times \boldsymbol{u} = 2\nu_r \nabla \times \boldsymbol{w} + \cdots, \tag{3.1}$$

$$\boldsymbol{w}_t + 4\nu_r \boldsymbol{w} = 2\nu_r \nabla \times \boldsymbol{u} + \cdots. \tag{3.2}$$

As derived from Theorem 2.1 regarding the PDE energy law (see (2.18)), one may discretize all four terms $\nu_r \nabla \times \nabla \times \boldsymbol{u}$, $2\nu_r \nabla \times \boldsymbol{w}$, $4\nu_r \boldsymbol{w}$, and $2\nu_r \nabla \times \boldsymbol{u}$ implicitly in order to acquire a complete square form $\|\nabla \times \boldsymbol{u} - 2\boldsymbol{w}\|^2$. Nonetheless, the implicit treatment of two cross terms $2\nu_r \nabla \times \boldsymbol{w}$ and $2\nu_r \nabla \times \boldsymbol{u}$ would result in a coupled scheme between the variables $\boldsymbol{u}$ and $\boldsymbol{w}$, which does not align with our goal of establishing a fully decoupled scheme in this paper.

Therefore, the two terms $2\nu_r \nabla \times \boldsymbol{w}$ and $2\nu_r \nabla \times \boldsymbol{u}$ might undergo some form of explicit discretization. However, this introduces a new challenge, notably the potential risk of failing to achieve unconditional energy stability. A similar scenario arises in numerous nonlinear systems that share similar linear coupling structures, such as the widely used decoupled second-order accurate schemes for the micropolar-Navier–Stokes (MNS) system that are conditionally stable [19, 29].

In this article, inspired by the ZEC approach [41, 42, 43], we deal with these terms as follows. We introduce a nonlocal variable $Q(t)$ and recall the following fact: the ODE with the form

$$Q_t = \mathfrak{a}(t)(1 - Q), \quad Q|_{t=0} = 1 \tag{3.3}$$

with any bounded function $\mathfrak{a}(t)$ only has a trivial solution of $Q(t) \equiv 1$. Thanks to this fact, we design an ODE that is in the same form of (3.3) for $Q(t)$, which reads as follows:

$$Q_t + 8\nu_r(\boldsymbol{w}, \boldsymbol{w})Q = 8\nu_r(\boldsymbol{w}, \boldsymbol{w}) + \underbrace{2\nu_r(\boldsymbol{w}, \nabla \times \boldsymbol{u}) - 2\nu_r(\nabla \times \boldsymbol{u}, \boldsymbol{w})}_{=0}, \quad Q|_{t=0} = 1, \tag{3.4}$$

where we fill in the right-hand side with two inner product terms. Due to the mutual cancellation of these two terms, (3.4) is equivalent to (3.3), which possesses a unique solution of $Q(t) \equiv 1$.

By using the auxiliary variable Q, we reformulate the system (3.1)–(3.2) as an equivalent form:

$$\boldsymbol{u}_t + \nu_r \nabla \times \nabla \times \boldsymbol{u} = 2\nu_r Q \nabla \times \boldsymbol{w} + \cdots, \tag{3.5}$$

$$\boldsymbol{w}_t + 4\nu_r \boldsymbol{w} = 2\nu_r Q \nabla \times \boldsymbol{u} + \cdots, \tag{3.6}$$

$$Q_t + 8\nu_r(\boldsymbol{w}, \boldsymbol{w})Q = 8\nu_r(\boldsymbol{w}, \boldsymbol{w}) + 2\nu_r(\boldsymbol{w}, \nabla \times \boldsymbol{u}) - 2\nu_r(\nabla \times \boldsymbol{u}, \boldsymbol{w}), \tag{3.7}$$

with $Q|_{t=0} = 1$. Note that in both (3.5) and (3.6), the two terms on the right are intentionally multiplied by the variable Q. Given that $Q \equiv 1$, the reformulated system (3.5)–(3.7) is entirely equivalent to the system (3.1)–(3.2).

In the following, we will briefly describe the design of the decoupled type scheme and elucidate the rationale behind the transformation of the system (3.1)–(3.2) into the more "*algorithm-friendly*" format (3.5)–(3.7), facilitated by the nonlocal variable Q. This approach allows us to easily achieve the desired decoupled scheme through straightforward explicit discretization methods for the coupled terms while preserving energy stability. While the primary focus of this study is on the second-order fully discrete scheme, we have opted to employ the first-order time marching scheme as an illustrative example due to its ability to offer a more straightforward and lucid demonstration of the energy stability proof. Let $N > 0$ denote the total

number of time steps; we define the time step size as $\delta t = [\frac{T}{N}]$ and set $t_n = n\delta t$. By denoting $d_t\psi^{n+1} = \frac{\psi^{n+1}-\psi^n}{\delta t}$, the first-order temporal discretization scheme for the system (3.5)–(3.7) reads as follows:

$$d_t\boldsymbol{u}^{n+1} + \nu_r\nabla\times\nabla\times\boldsymbol{u}^{n+1} = 2\nu_r Q^{n+1}\nabla\times\boldsymbol{w}^n + \cdots, \tag{3.8}$$

$$d_t\boldsymbol{w}^{n+1} + 4\nu_r\boldsymbol{w}^{n+1} = 2\nu_r Q^{n+1}\nabla\times\boldsymbol{u}^n + \cdots, \tag{3.9}$$

$$\begin{aligned} d_tQ^{n+1} + 8\nu_r(\boldsymbol{w}^n,\boldsymbol{w}^n)Q^{n+1} &= 8\nu_r(\boldsymbol{w}^n,\boldsymbol{w}^{n+1}) + 2\nu_r(\boldsymbol{w}^n,\nabla\times\boldsymbol{u}^{n+1}) \\ &\quad - 2\nu_r(\nabla\times\boldsymbol{u}^n,\boldsymbol{w}^{n+1}). \end{aligned} \tag{3.10}$$

By taking the L^2 inner product of $\boldsymbol{u}^{n+1}$ with (3.8) and of $\boldsymbol{w}^{n+1}$ with (3.9), multiplying (3.10) with Q^{n+1}, combining the three obtained equations, and using the Hölder and Cauchy–Schwarz inequalities (since the details on deriving energy stability will be discussed in Theorem 4.1, we provide a brief outline here), we obtain

$$\|\boldsymbol{u}^{n+1}\|^2 + \|\boldsymbol{w}^{n+1}\|^2 + |Q^{n+1}|^2 \le \|\boldsymbol{u}^n\|^2 + \|\boldsymbol{w}^n\|^2 + |Q^n|^2, \tag{3.11}$$

which implies the energy stability. In the scheme presented in (3.8)–(3.10), it's important to note that the direct coupling of $\boldsymbol{u}$-$\boldsymbol{w}$ is eliminated, resulting in a coupling relationship of $\boldsymbol{u}$-Q and $\boldsymbol{w}$-Q. By leveraging the nonlocal characteristics of the variable Q and applying a nonlocal splitting method akin to the ZEC approach, we can achieve a fully decoupled implementation, with further details provided in section 4.2.

Remark 3.1. Indeed, similar linear coupling structures have surfaced in the micropolar-Navier–Stokes (MNS) system [19, 29, 36, 48], sine-Gordon equations [38], Hamiltonian system of perturbed Schrödinger equations [9], etc. Therefore, we abstract the above methods into a framework-type approach, providing a convenient tool for the interested reader to address similar models.

We denote $\mathfrak{D}_1$ and $\mathfrak{D}_2$ by two differential operators. The mathematical structure behind (3.1)–(3.2) can be expressed as

$$\Phi_t + a^2\mathfrak{D}_1\mathfrak{D}_1\Phi = \eta ab\mathfrak{D}_1\mathfrak{D}_2\Psi, \tag{3.12}$$

$$\Psi_t + b^2\mathfrak{D}_2\mathfrak{D}_2\Psi = (2-\eta)ab\mathfrak{D}_2\mathfrak{D}_1\Phi, \tag{3.13}$$

where $0<\eta<2$, a, b are two positive parameters. Taking the L^2 inner product of Φ with (3.12) and of Ψ with (3.13) and using integration by parts, we derive

$$\begin{aligned} &\frac{1}{2}\frac{d}{dt}\|\Phi\|^2 + a^2\|\mathfrak{D}_1\Phi\|^2 = \eta ab(\mathfrak{D}_2\Psi,\mathfrak{D}_1\Phi), \\ &\frac{1}{2}\frac{d}{dt}\|\Psi\|^2 + b^2\|\mathfrak{D}_2\Psi\|^2 = (2-\eta)ab(\mathfrak{D}_1\Phi,\mathfrak{D}_2\Psi). \end{aligned}$$

Summing up the above equations, we obtain $\frac{1}{2}\frac{d}{dt}(\|\Phi\|^2+\|\Psi\|^2)+\|a\mathfrak{D}_1\Phi-b\mathfrak{D}_2\Psi\|^2=0$. We reformulate (3.12)–(3.13) into an equivalent system by coupling an ODE, which reads as follows: given $Q|_{t=0}=1$,

$$\begin{cases} \Phi_t + a^2\mathfrak{D}_1\mathfrak{D}_1\Phi = Q\eta ab\mathfrak{D}_1\mathfrak{D}_2\Psi, \\ \Psi_t + b^2\mathfrak{D}_2\mathfrak{D}_2\Psi = Q(2-\eta)ab\mathfrak{D}_2\mathfrak{D}_1\Phi, \\ Q_t + \alpha\|\mathfrak{D}_1\Phi\|^2Q = \alpha(\mathfrak{D}_1\Phi,\mathfrak{D}_1\Phi) + \eta ab(\mathfrak{D}_1\Phi,\mathfrak{D}_2\Psi) - \eta ab(\mathfrak{D}_2\Psi,\mathfrak{D}_1\Phi), \end{cases} \tag{3.14}$$

where α is a positive parameter that will be determined later. Visibly, the ODE in (3.14) adheres to (3.3) with $\mathfrak{a}=\alpha\|\mathfrak{D}_1\Phi\|^2$. We discretize the system (3.14) as follows:

$$
\begin{cases}
d_t\Phi^{n+1}+a^2\mathfrak{D}_1\mathfrak{D}_1\Phi^{n+1}=Q^{n+1}\eta ab\mathfrak{D}_1\mathfrak{D}_2\Psi^n,\\
d_t\Psi^{n+1}+b^2\mathfrak{D}_2\mathfrak{D}_2\Psi^{n+1}=Q^{n+1}(2-\eta)ab\mathfrak{D}_2\mathfrak{D}_1\Phi^n,\\
d_tQ^{n+1}+\alpha\|\mathfrak{D}_1\Phi^n\|^2Q^{n+1}=\alpha(\mathfrak{D}_1\Phi^n,\mathfrak{D}_1\Phi^{n+1})+\eta ab(\mathfrak{D}_1\Phi^n,\mathfrak{D}_2\Psi^{n+1})\\
\qquad\qquad\qquad\qquad\qquad\qquad -\eta ab(\mathfrak{D}_2\Psi^n,\mathfrak{D}_1\Phi^{n+1}).
\end{cases}
\tag{3.15}
$$

Taking the L^2 inner product of Φ^{n+1} and Ψ^{n+1} with the first and second equations in (3.15), respectively, multiplying Q^{n+1} on the discrete ODE, and summing them up, we have

$$
\begin{aligned}
&\frac{1}{2\delta t}(\|\Phi^{n+1}\|^2-\|\Phi^n\|^2+\|\Phi^{n+1}-\Phi^n\|^2)+\frac{1}{2\delta t}(\|\Psi^{n+1}\|^2-\|\Psi^n\|^2+\|\Psi^{n+1}-\Psi^n\|^2)\\
&\quad+\frac{1}{2\delta t}(|Q^{n+1}|^2-|Q^n|^2+|Q^{n+1}-Q^n|^2)+a^2\|\mathfrak{D}_1\Phi^{n+1}\|^2+b^2\|\mathfrak{D}_2\Psi^{n+1}\|^2\\
&\quad+\alpha|Q^{n+1}|^2\|\mathfrak{D}_1\Phi^n\|^2\\
&=Q^{n+1}2ab(\mathfrak{D}_1\Phi^n,\mathfrak{D}_2\Psi^{n+1})+Q^{n+1}\alpha(\mathfrak{D}_1\Phi^n,\mathfrak{D}_1\Phi^{n+1})\\
&\le 2ab|Q^{n+1}|\|\mathfrak{D}_1\Phi^n\|\|\mathfrak{D}_2\Psi^{n+1}\|+\alpha|Q^{n+1}|\|\mathfrak{D}_1\Phi^n\|\|\mathfrak{D}_1\Phi^{n+1}\|\\
&\le b^2\|\mathfrak{D}_2\Psi^{n+1}\|^2+a^2|Q^{n+1}|^2\|\mathfrak{D}_1\Phi^n\|^2+a^2\|\mathfrak{D}_1\Phi^{n+1}\|^2+\frac{1}{4a^2}\alpha^2|Q^{n+1}|^2\|\mathfrak{D}_1\Phi^n\|^2,
\end{aligned}
$$

where integration by parts and the Hölder and Cauchy-Schwarz inequalities are also utilized. If we choose α such that $\frac{1}{4a^2}\alpha^2-\alpha+a^2=(\frac{1}{2a}\alpha-a)^2\le 0$, which has a unique solution $\alpha=2a^2$, we have the stability

$$
\|\Phi^{n+1}\|^2+\|\Psi^{n+1}\|^2+|Q^{n+1}|^2\le\|\Phi^n\|^2+\|\Psi^n\|^2+|Q^n|^2.
$$

If setting $\Phi=\boldsymbol{w}$, $\Psi=\boldsymbol{u}$, $\mathcal{D}_1=I$, $\mathcal{D}_2=\nabla\times$, $a=2\sqrt{\nu_r}$, $b=\sqrt{\nu_r}$, $\eta=1$, and $\alpha=8\nu_r$ in (3.12)–(3.13), in (3.14), and in (3.15), respectively, we recover equations (3.1)–(3.2), system (3.5)–(3.7), and scheme (3.8)–(3.10), respectively. In contrast, utilizing our framework developed above, the unconditionally energy-stable scheme with second-order accuracy and decoupled manner could be designed, this will be detailed in section 4.

3.1.2. $\boldsymbol{m}$-$\boldsymbol{\varphi}$ linear coupling. In this subsection, we address the linear coupling between $\boldsymbol{m}$ and φ that appears in (2.4)–(2.5). It is worth noting that the Shliomis FHD model also exhibits similar couplings between these two variables. In our previous work [47], we derive an equivalent form of the magnetic potential equation to resolve this linear coupling in the Shliomis FHD model. In this paper, we extend a similar approach to the Rosensweig FHD model. We also refer the reader to [17] for the idea of reformulated approach. The procedure is as detailed below.

By taking the time derivative of (2.5) and multiplying (2.5) by $\frac{1}{\tau}$, respectively, we get the following two equations:

$$
-\Delta\varphi_t=\nabla\cdot\boldsymbol{m}_t-\nabla\cdot\boldsymbol{h}_b,\quad -\frac{1}{\tau}\Delta\varphi=\frac{1}{\tau}\nabla\cdot\boldsymbol{m}-\frac{1}{\tau}\nabla\cdot\boldsymbol{h}_a.
$$

By taking the L^2 inner product of the above equations with ψ for any $\psi\in H^1(\Omega)\cap L_0^2(\Omega)$, we derive their weak forms as

$$
(\nabla\varphi_t,\nabla\psi)+(\boldsymbol{m}_t,\nabla\psi)=(\boldsymbol{h}_b,\nabla\psi),\quad \frac{1}{\tau}(\nabla\varphi,\nabla\psi)+\frac{1}{\tau}(\boldsymbol{m},\nabla\psi)=\frac{1}{\tau}(\boldsymbol{h}_a,\nabla\psi).
\tag{3.16}
$$

Additionally, by taking the L^2 inner product of (2.4) with $\nabla\psi$, we derive

$$\frac{\chi_0}{\tau}(\nabla\varphi,\nabla\psi)-((\boldsymbol{u}\cdot\nabla)\boldsymbol{m},\nabla\psi)+(\boldsymbol{w}\times\boldsymbol{m},\nabla\psi)=(\boldsymbol{m}_t,\nabla\psi)+\frac{1}{\tau}(\boldsymbol{m},\nabla\psi). \tag{3.17}$$

By taking the summation of the three equations in (3.16)–(3.17), we obtain a new equation as

$$\begin{aligned}(\nabla\varphi_t,\nabla\psi)+\frac{1}{\tau}(\nabla\varphi,\nabla\psi)+\frac{\chi_0}{\tau}(\nabla\varphi,\nabla\psi)-((\boldsymbol{u}\cdot\nabla)\boldsymbol{m},\nabla\psi)+(\boldsymbol{w}\times\boldsymbol{m},\nabla\psi)\\ =\frac{1}{\tau}(\boldsymbol{h}_a,\nabla\psi)+(\boldsymbol{h}_b,\nabla\psi),\end{aligned} \tag{3.18}$$

which is used to replace the magnetostatic equation (2.5) to solve φ. We also present the weak form of the magnetization equation for $\boldsymbol{m}$ that reads as

$$(\boldsymbol{m}_t,\boldsymbol{n})+\frac{1}{\tau}(\boldsymbol{m},\boldsymbol{n})+((\boldsymbol{u}\cdot\nabla)\boldsymbol{m},\boldsymbol{n})=(\boldsymbol{w}\times\boldsymbol{m},\boldsymbol{n})+\frac{\chi_0}{\tau}(\boldsymbol{h},\boldsymbol{n}),\quad\forall\boldsymbol{n}\in\boldsymbol{H}^1(\Omega). \tag{3.19}$$

It is noteworthy that the linear coupling between $\boldsymbol{m}$ and φ in (3.18)–(3.19) is eliminated in the new equation (3.18) for the variable φ. Although two nonlinear coupling terms $((\boldsymbol{u}\cdot\nabla)\boldsymbol{m},\nabla\psi)$ and $(\boldsymbol{w}\times\boldsymbol{m},\nabla\psi)$ are further introduced, we note that they actually satisfy the so-called "zero-energy-contribution" property when choosing suitable test functions of ψ and associating the results with other terms, which then can be effectively discretized by the ZEC approach; see the detailed discussion in section 3.2.

3.2. Nonlinear couplings. This subsection addresses the multitude of nonlinear coupling terms. To do so, it is necessary to establish the weak form of the entire governing system.

In the momentum equation (2.1), the weak form of the Kelvin force term can be expressed as $\mu((\boldsymbol{m}\cdot\nabla)\boldsymbol{h},\boldsymbol{v})$ after taking the L^2 inner product with a test function $\boldsymbol{v}\in\boldsymbol{H}_0^1(\Omega)$. When employing the finite element method for spatial discretization, this term will introduce boundary integrations involving jump and average terms across interior boundaries due to the fact that $\boldsymbol{h}=\nabla\varphi$; see [20]. To avoid such a challenging issue, using the fact $\nabla\times\boldsymbol{h}=0$ and integration by parts, we rewrite the term $\mu((\boldsymbol{m}\cdot\nabla)\boldsymbol{h},\boldsymbol{v})$ as

$$\mu((\boldsymbol{m}\cdot\nabla)\boldsymbol{h},\boldsymbol{v})=\mu((\boldsymbol{v}\cdot\nabla)\boldsymbol{h},\boldsymbol{m})=-\mu((\boldsymbol{v}\cdot\nabla)\boldsymbol{m},\boldsymbol{h})-\mu((\nabla\cdot\boldsymbol{v})\boldsymbol{m},\boldsymbol{h}), \tag{3.20}$$

where no spatial derivatives are applied on $\boldsymbol{h}$. We denote $\boldsymbol{X}=\boldsymbol{H}_0^1(\Omega)\times L_0^2(\Omega)\times\boldsymbol{H}_0^1(\Omega)\times H^1(\Omega)\cap L_0^2(\Omega)\times\boldsymbol{H}^1(\Omega)$.

Hence, by applying (3.20) for the fluid momentum equation, combining with the weak form given in (3.18), (3.19) for φ and $\boldsymbol{m}$, and taking the appropriate weak form for (2.2), (2.3), the weak form for the entire system of the Rosensweig FHD model reads as follows: find $(\boldsymbol{u}(t),p(t),\boldsymbol{w}(t),\varphi(t),\boldsymbol{m}(t))\in\boldsymbol{X}$ such that for all $(\boldsymbol{v},q,\boldsymbol{Z},\psi,\boldsymbol{n})\in\boldsymbol{X}$, there hold

(3.21)
$$
\begin{cases}
(\boldsymbol{u}_t,\boldsymbol{v})+\nu(\nabla\boldsymbol{u},\nabla\boldsymbol{v})+\nu_r(\nabla\times\boldsymbol{u},\nabla\times\boldsymbol{v})+\nu_r(\nabla\cdot\boldsymbol{u},\nabla\cdot\boldsymbol{v})+((\boldsymbol{u}\cdot\nabla)\boldsymbol{u},\boldsymbol{v})-(p,\nabla\cdot\boldsymbol{v})\\
\qquad=2\nu_r(\boldsymbol{w},\nabla\times\boldsymbol{v})-\mu((\boldsymbol{v}\cdot\nabla)\boldsymbol{m},\boldsymbol{h})-\mu((\nabla\cdot\boldsymbol{v})\boldsymbol{m},\boldsymbol{h}),\\
(\nabla\cdot\boldsymbol{u},q)=0,\\
\zeta(\boldsymbol{w}_t,\boldsymbol{Z})+c_1(\nabla\boldsymbol{w},\nabla\boldsymbol{Z})+c_2(\nabla\cdot\boldsymbol{w},\nabla\cdot\boldsymbol{Z})+4\nu_r(\boldsymbol{w},\boldsymbol{Z})+\zeta((\boldsymbol{u}\cdot\nabla)\boldsymbol{w},\boldsymbol{Z})\\
\qquad=2\nu_r(\nabla\times\boldsymbol{u},\boldsymbol{Z})+\mu(\boldsymbol{m}\times\boldsymbol{h},\boldsymbol{Z}),\\
(\nabla\varphi_t,\nabla\psi)+\dfrac{1}{\tau}(\nabla\varphi,\nabla\psi)+\dfrac{\chi_0}{\tau}(\nabla\varphi,\nabla\psi)-((\boldsymbol{u}\cdot\nabla)\boldsymbol{m},\nabla\psi)+(\boldsymbol{w}\times\boldsymbol{m},\nabla\psi)\\
\qquad=\dfrac{1}{\tau}(\boldsymbol{h}_a,\nabla\psi)+(\boldsymbol{h}_b,\nabla\psi),\\
(\boldsymbol{m}_t,\boldsymbol{n})+\dfrac{1}{\tau}(\boldsymbol{m},\boldsymbol{n})+((\boldsymbol{u}\cdot\nabla)\boldsymbol{m},\boldsymbol{n})=(\boldsymbol{w}\times\boldsymbol{m},\boldsymbol{n})+\dfrac{\chi_0}{\tau}(\boldsymbol{h},\boldsymbol{n}).
\end{cases}
$$

As can be seen from Theorem 2.1, the energy stability of the PDE system relies on the fact that a considerable number of nonlinear terms exhibit the "zero energy contribution" property, namely, these terms are either cancelled by other terms or simply equal to zero when the inner product of a particular variable is executed; see (2.19)–(2.21). This fact reminds us that we can apply the recently developed ZEC approach [41, 42, 43] to obtain a decoupled-type scheme by introducing a nonlocal auxiliary variable and designing the relevant ODE based on the zero equalities (2.19)–(2.21). Furthermore, it is important to mention that the reformulation implemented to account for the linear couplings between $\boldsymbol{m}$ and φ adheres to a comparable approach. As a result, we proceed by incorporating specific zero-valued terms into (3.4), thereby enabling the construction of a comprehensive ODE capable of simultaneously accommodating linear and nonlinear coupling terms. Namely, we further reformulate the ODE (3.4) to an equivalent form that reads as

(3.22)
$$
\begin{cases}
Q_t+8\nu_r(\boldsymbol{w},\boldsymbol{w})Q=8\nu_r(\boldsymbol{w},\boldsymbol{w})+2\nu_r(\boldsymbol{w},\nabla\times\boldsymbol{u})-2\nu_r(\nabla\times\boldsymbol{u},\boldsymbol{w})\\
\qquad\qquad+((\boldsymbol{u}\cdot\nabla)\boldsymbol{u},\boldsymbol{u})+\zeta((\boldsymbol{u}\cdot\nabla)\boldsymbol{w},\boldsymbol{w})+\dfrac{\mu}{\chi_0}((\boldsymbol{u}\cdot\nabla)\boldsymbol{m},\boldsymbol{m})-\dfrac{\mu}{\chi_0}(\boldsymbol{w}\times\boldsymbol{m},\boldsymbol{m})\\
\qquad\qquad+\mu(\boldsymbol{w}\times\boldsymbol{m},\nabla\varphi)-\mu(\boldsymbol{m}\times\nabla\varphi,\boldsymbol{w})\\
\qquad\qquad+\mu((\boldsymbol{u}\cdot\nabla)\boldsymbol{m},\nabla\varphi)-\mu((\boldsymbol{u}\cdot\nabla)\boldsymbol{m},\nabla\varphi)+\mu((\nabla\cdot\boldsymbol{u})\boldsymbol{m},\nabla\varphi),
\end{cases}
$$

with $Q|_{t=0}=1$. It is noteworthy that the terms in the first line on the right-hand side of (3.22) are taken from (3.4); each term from the second line is zero-valued from (2.19); the two terms in the third line cancel each other out to yield zero, mirroring a similar behavior observed in the initial two items of the fourth line; and the final item is also zero-valued in accordance with the divergence-free condition. As a result, the ODE (3.22) remains equivalent to the ODE (3.4), and it has a trivial solution of $Q\equiv 1$. Next, we will further use the nonlocal variable Q to perform the equivalent modification to the nonlinear couplings in the weak form of the entire system of (2.1)–(2.7).

Using the nonlocal variable and its associated ODE (3.22), we reformulate the weak form (3.21) into an equivalent system that reads as follows: given initial data $(\boldsymbol{u}_0,\ \boldsymbol{w}_0,\ \boldsymbol{m}_0,\ Q_0)$, find $(\boldsymbol{u},p,\boldsymbol{w},\varphi,\boldsymbol{m},Q)\in\boldsymbol{X}\times\mathbb{R}$ such that for all $(\boldsymbol{v},q,\boldsymbol{Z},\psi,\boldsymbol{n})\in\boldsymbol{X}$, there hold

(3.23)
$$(\boldsymbol{u}_t,\boldsymbol{v})+\nu(\nabla\boldsymbol{u},\nabla\boldsymbol{v})+\nu_r(\nabla\times\boldsymbol{u},\nabla\times\boldsymbol{v})+\nu_r(\nabla\cdot\boldsymbol{u},\nabla\cdot\boldsymbol{v})+Q((\boldsymbol{u}\cdot\nabla)\boldsymbol{u},\boldsymbol{v})-(p,\nabla\cdot\boldsymbol{v})$$
$$=2\nu_rQ(\boldsymbol{w},\nabla\times\boldsymbol{v})-\mu Q((\boldsymbol{v}\cdot\nabla)\boldsymbol{m},\boldsymbol{h})-\mu Q((\nabla\cdot\boldsymbol{v})\boldsymbol{m},\boldsymbol{h}),$$
(3.24)
$$(\nabla\cdot\boldsymbol{u},q)=0,$$
(3.25)
$$\zeta(\boldsymbol{w}_t,\boldsymbol{Z})+c_1(\nabla\boldsymbol{w},\nabla\boldsymbol{Z})+c_2(\nabla\cdot\boldsymbol{w},\nabla\cdot\boldsymbol{Z})+4\nu_r(\boldsymbol{w},\boldsymbol{Z})+\zeta Q((\boldsymbol{u}\cdot\nabla)\boldsymbol{w},\boldsymbol{Z})$$
$$=2\nu_rQ(\nabla\times\boldsymbol{u},\boldsymbol{Z})+\mu Q(\boldsymbol{m}\times\boldsymbol{h},\boldsymbol{Z}),$$
(3.26)
$$(\nabla\varphi_t,\nabla\psi)+\frac{1}{\tau}(\nabla\varphi,\nabla\psi)+\frac{\chi_0}{\tau}(\nabla\varphi,\nabla\psi)-Q((\boldsymbol{u}\cdot\nabla)\boldsymbol{m},\nabla\psi)+Q(\boldsymbol{w}\times\boldsymbol{m},\nabla\psi)$$
(3.27)
$$=\frac{1}{\tau}(\boldsymbol{h}_a,\nabla\psi)+(\boldsymbol{h}_b,\nabla\psi),$$
(3.28)
$$(\boldsymbol{m}_t,\boldsymbol{n})+\frac{1}{\tau}(\boldsymbol{m},\boldsymbol{n})+Q((\boldsymbol{u}\cdot\nabla)\boldsymbol{m},\boldsymbol{n})=Q(\boldsymbol{w}\times\boldsymbol{m},\boldsymbol{n})+\frac{\chi_0}{\tau}(\boldsymbol{h},\boldsymbol{n}),$$
(3.29)
$$Q_t+8\nu_r(\boldsymbol{w},\boldsymbol{w})Q=8\nu_r(\boldsymbol{w},\boldsymbol{w})+2\nu_r(\boldsymbol{w},\nabla\times\boldsymbol{u})-2\nu_r(\nabla\times\boldsymbol{u},\boldsymbol{w})$$
$$+((\boldsymbol{u}\cdot\nabla)\boldsymbol{u},\boldsymbol{u})+\zeta((\boldsymbol{u}\cdot\nabla)\boldsymbol{w},\boldsymbol{w})+\frac{\mu}{\chi_0}((\boldsymbol{u}\cdot\nabla)\boldsymbol{m},\boldsymbol{m})-\frac{\mu}{\chi_0}(\boldsymbol{w}\times\boldsymbol{m},\boldsymbol{m})$$
$$+\mu(\boldsymbol{w}\times\boldsymbol{m},\nabla\varphi)-\mu(\boldsymbol{m}\times\nabla\varphi,\boldsymbol{w})$$
$$+\mu((\boldsymbol{u}\cdot\nabla)\boldsymbol{m},\nabla\varphi)-\mu((\boldsymbol{u}\cdot\nabla)\boldsymbol{m},\nabla\varphi)+\mu((\nabla\cdot\boldsymbol{u})\boldsymbol{m},\nabla\varphi).$$

Remark 3.2. It is crucial to note that the system (3.23)–(3.29) is identical to (3.21), as $Q\equiv 1$. Although the resultant system (3.23)–(3.29) appears to be an ongoing series of mundane reconstructions intended to further complicate the original model (3.21), this is actually an "algorithm-friendly" format. In other words, the construction of the scheme is remarkably uncomplicated and practical, as each linear and nonlinear coupling term (Q-multiplying terms) can be explicitly discretized while still maintaining the energy stability. In addition, the obtained scheme's implementation will be rather efficient, requiring only the solution of a handful of independent elliptic/parabolic equations with constant coefficients at each time step without any additional complexity. The following section will outline these numerical benefits.

The system (3.23)–(3.29) is also accompanied by a modified energy estimate, as follows.

THEOREM 3.1. *The system* (3.23)–(3.29) *admits the energy law in the sense that*
$$\frac{d}{dt}\left(\frac{1}{2}\|\boldsymbol{u}\|^2+\frac{\zeta}{2}\|\boldsymbol{w}\|^2+\frac{\mu}{2}\|\boldsymbol{h}\|^2+\frac{\mu}{2\chi_0}\|\boldsymbol{m}\|^2+\frac{1}{2}|Q|^2\right)$$
$$+\nu\|\nabla\boldsymbol{u}\|^2+\nu_r\|\nabla\cdot\boldsymbol{u}\|^2+c_1\|\nabla\boldsymbol{w}\|^2+c_2\|\nabla\cdot\boldsymbol{w}\|^2+\frac{\mu}{2\tau}\|\boldsymbol{h}\|^2+\frac{3\mu}{4\chi_0\tau}\|\boldsymbol{m}\|^2$$
$$\le\frac{\mu}{\tau}\|\boldsymbol{h}_a\|^2+\tau\mu\|\boldsymbol{h}_b\|^2.$$

Since it is similar to the proof of the discrete energy law in Theorem 4.1 of the numerical scheme, we omit it due to page limitation.

4. Fully discrete finite element numerical scheme. We introduce some conforming finite element spaces

$$\boldsymbol{V}_h \subset \boldsymbol{H}_0^1(\Omega),\ Q_h \subset L_0^2(\Omega)\cap H^1(\Omega),\ \boldsymbol{\mathcal{Z}}_h \subset \boldsymbol{H}_0^1(\Omega),\ \Psi_h \subset L_0^2(\Omega)\cap H^1(\Omega),\ \boldsymbol{N}_h \subset \boldsymbol{H}^1(\Omega),$$

and we assume $(\boldsymbol{V}_h, Q_h)$ satisfy the following *inf-sup* condition [10]: $\beta_0\|q\| \le \sup_{\boldsymbol{v}\in\boldsymbol{V}_h} \frac{(\nabla\cdot\boldsymbol{v},q)}{\|\nabla\boldsymbol{v}\|}$ $\forall q \in Q_h$, where the constant β_0 only depends on Ω. So far, we have made all necessary preparations for the construction of our scheme for the target model (2.1)–(2.7).

4.1. Numerical scheme. We denote $D_t\psi^{n+1} = \frac{3\psi^{n+1}-4\psi^n+\psi^{n-1}}{2\delta t}$, $\tilde{D}_t\psi^{n+1} = \frac{3\tilde{\psi}^{n+1}-4\psi^n+\psi^{n-1}}{2\delta t}$, $\phi^* = 2\phi^n - \phi^{n-1}$. The fully discrete numerical scheme for (3.23)–(3.29) reads as follows: find $\tilde{\boldsymbol{u}}^{n+1} \in \boldsymbol{V}_h$, $p^{n+1} \in Q_h$, $\boldsymbol{u}^{n+1} \in \boldsymbol{V}_h + \nabla Q_h$, $\boldsymbol{w}^{n+1} \in \boldsymbol{\mathcal{Z}}_h$, $\varphi^{n+1} \in \Psi_h$, $\boldsymbol{m}^{n+1} \in \boldsymbol{N}_h$, $Q^{n+1} \in \mathbb{R}$; there hold

(4.1)
$$\begin{aligned}&(\tilde{D}_t\boldsymbol{u}^{n+1},\boldsymbol{v}) + \nu(\nabla\tilde{\boldsymbol{u}}^{n+1},\nabla\boldsymbol{v}) + \nu_r(\nabla\times\tilde{\boldsymbol{u}}^{n+1},\nabla\times\boldsymbol{v}) + \nu_r(\nabla\cdot\tilde{\boldsymbol{u}}^{n+1},\nabla\cdot\boldsymbol{v})\\ &\quad + Q^{n+1}((\boldsymbol{u}^*\cdot\nabla)\boldsymbol{u}^*,\boldsymbol{v}) + (\nabla p^n,\boldsymbol{v})\\ &\quad = 2\nu_r Q^{n+1}(\boldsymbol{w}^*,\nabla\times\boldsymbol{v}) - \mu Q^{n+1}((\boldsymbol{v}\cdot\nabla)\boldsymbol{m}^*,\boldsymbol{h}^*) - \mu Q^{n+1}((\nabla\cdot\boldsymbol{v})\boldsymbol{m}^*,\boldsymbol{h}^*),\end{aligned}$$

(4.2)
$$(\nabla p^{n+1},\nabla q) = -\frac{3}{2\delta t}(\nabla\cdot\tilde{\boldsymbol{u}}^{n+1},q) + (\nabla p^n,\nabla q),$$

(4.3)
$$\boldsymbol{u}^{n+1} = \tilde{\boldsymbol{u}}^{n+1} - \frac{2\delta t}{3}\nabla p^{n+1} + \frac{2\delta t}{3}\nabla p^n,$$

(4.4)
$$\begin{aligned}&\zeta(D_t\boldsymbol{w}^{n+1},\boldsymbol{Z}) + c_1(\nabla\boldsymbol{w}^{n+1},\nabla\boldsymbol{Z}) + c_2(\nabla\cdot\boldsymbol{w}^{n+1},\nabla\cdot\boldsymbol{Z}) + 4\nu_r(\boldsymbol{w}^{n+1},\boldsymbol{Z})\\ &\quad + \zeta Q^{n+1}((\boldsymbol{u}^*\cdot\nabla)\boldsymbol{w}^*,\boldsymbol{Z}) = 2\nu_r Q^{n+1}(\nabla\times\boldsymbol{u}^*,\boldsymbol{Z}) + \mu Q^{n+1}(\boldsymbol{m}^*\times\boldsymbol{h}^*,\boldsymbol{Z}),\end{aligned}$$

(4.5)
$$\begin{aligned}&(\nabla D_t\varphi^{n+1},\nabla\psi) + \frac{1}{\tau}(\nabla\varphi^{n+1},\nabla\psi) + \frac{\chi_0}{\tau}(\nabla\varphi^{n+1},\nabla\psi) - Q^{n+1}((\boldsymbol{u}^*\cdot\nabla)\boldsymbol{m}^*,\nabla\psi)\\ &\quad + Q^{n+1}(\boldsymbol{w}^*\times\boldsymbol{m}^*,\nabla\psi) = \frac{1}{\tau}(\boldsymbol{h}_a^{n+1},\nabla\psi) + (\boldsymbol{h}_b^{n+1},\nabla\psi),\end{aligned}$$

(4.6)
$$\begin{aligned}&(D_t\boldsymbol{m}^{n+1},\boldsymbol{n}) + \frac{1}{\tau}(\boldsymbol{m}^{n+1},\boldsymbol{n}) + Q^{n+1}((\boldsymbol{u}^*\cdot\nabla)\boldsymbol{m}^*,\boldsymbol{n})\\ &\quad = Q^{n+1}(\boldsymbol{w}^*\times\boldsymbol{m}^*,\boldsymbol{n}) + \frac{\chi_0}{\tau}(\boldsymbol{h}^{n+1},\boldsymbol{n}),\end{aligned}$$

(4.7)
$$\begin{aligned}&D_tQ^{n+1} + 8\nu_r(\boldsymbol{w}^*,\boldsymbol{w}^*)Q^{n+1}\\ &\quad = 8\nu_r(\boldsymbol{w}^*,\boldsymbol{w}^{n+1}) + 2\nu_r(\boldsymbol{w}^*,\nabla\times\tilde{\boldsymbol{u}}^{n+1}) - 2\nu_r(\nabla\times\boldsymbol{u}^*,\boldsymbol{w}^{n+1})\\ &\qquad + ((\boldsymbol{u}^*\cdot\nabla)\boldsymbol{u}^*,\tilde{\boldsymbol{u}}^{n+1}) + \zeta((\boldsymbol{u}^*\cdot\nabla)\boldsymbol{w}^*,\boldsymbol{w}^{n+1}) + \frac{\mu}{\chi_0}((\boldsymbol{u}^*\cdot\nabla)\boldsymbol{m}^*,\boldsymbol{m}^{n+1})\\ &\qquad - \frac{\mu}{\chi_0}(\boldsymbol{w}^*\times\boldsymbol{m}^*,\boldsymbol{m}^{n+1}) + \mu(\boldsymbol{w}^*\times\boldsymbol{m}^*,\nabla\varphi^{n+1}) - \mu(\boldsymbol{m}^*\times\nabla\varphi^*,\boldsymbol{w}^{n+1})\\ &\qquad + \mu((\tilde{\boldsymbol{u}}^{n+1}\cdot\nabla)\boldsymbol{m}^*,\nabla\varphi^*) - \mu((\boldsymbol{u}^*\cdot\nabla)\boldsymbol{m}^*,\nabla\varphi^{n+1}) + \mu((\nabla\cdot\tilde{\boldsymbol{u}}^{n+1})\boldsymbol{m}^*,\nabla\varphi^*)\end{aligned}$$

for all $\boldsymbol{v}\in\boldsymbol{V}_h$, $q\in Q_h$, $\boldsymbol{Z}\in\boldsymbol{\mathcal{Z}}_h$, $\psi\in\Psi_h$, $\boldsymbol{n}\in\boldsymbol{N}_h$, where $\boldsymbol{h}^* = \nabla\varphi^*$, $\boldsymbol{h}^{n+1} = \nabla\varphi^{n+1}$.

We explain the algorithm development strategy in the following remarks.

Remark 4.1. The second-order pressure projection method [11, 32] is used to deal with the hydrodynamics equation that includes the $\boldsymbol{u}$-p linear coupling, where $\tilde{\boldsymbol{u}}^{n+1}$ accounts for the intermediate velocity, and the $\boldsymbol{u}^{n+1}$ means the final velocity that satisfies the discrete divergence-free condition. To see this, we take the L^2 inner product of (4.3) with ∇q and use (4.2) to obtain [46]

$$(\boldsymbol{u}^{n+1}, \nabla q) = 0 \ \forall q \in Q_h. \tag{4.8}$$

Remark 4.2. The discretization of the time derivatives is accomplished through the utilization of the second-order backward difference formula (BDF2). In equations (4.1)–(4.6), a discretization technique known as implicit-explicit discretization is employed for the Q-multiplying terms. Specifically, the variable Q is discretized implicitly, while the remaining terms are discretized explicitly.

We define

$$\begin{aligned}
E_h^{n+1} &= \frac{1}{4}(\|\boldsymbol{u}^{n+1}\|^2 + \|2\boldsymbol{u}^{n+1} - \boldsymbol{u}^n\|^2) + \frac{\zeta}{4}(\|\boldsymbol{w}^{n+1}\|^2 + \|2\boldsymbol{w}^{n+1} - \boldsymbol{w}^n\|^2) \\
&\quad + \frac{\mu}{4}(\|\boldsymbol{h}^{n+1}\|^2 + \|2\boldsymbol{h}^{n+1} - \boldsymbol{h}^n\|^2) + \frac{\mu}{4\chi_0}(\|\boldsymbol{m}^{n+1}\|^2 + \|2\boldsymbol{m}^{n+1} - \boldsymbol{m}^n\|^2) \\
&\quad + \frac{1}{4}(|Q^{n+1}|^2 + |2Q^{n+1} - Q^n|^2) + \frac{\delta t^2}{3}\|\nabla p^{n+1}\|^2, \\
D_h^{n+1} &= \nu\|\nabla\tilde{\boldsymbol{u}}^{n+1}\|^2 + \nu_r\|\nabla\cdot\tilde{\boldsymbol{u}}^{n+1}\|^2 + c_1\|\nabla\boldsymbol{w}^{n+1}\|^2 + c_2\|\nabla\cdot\boldsymbol{w}^{n+1}\|^2 + \frac{\mu}{2\tau}\|\boldsymbol{h}^{n+1}\|^2 \\
&\quad + \frac{3\mu}{4\tau\chi_0}\|\boldsymbol{m}^{n+1}\|^2.
\end{aligned}$$

We further show that the scheme (4.1)–(4.7) holds the energy estimate unconditionally, as follows.

THEOREM 4.1. *The scheme* (4.1)–(4.7) *is unconditionally energy stable in the sense that*

$$d_t E_h^{n+1} + D_h^{n+1} \le \frac{\mu}{\tau}\|\boldsymbol{h}_a^{n+1}\|^2 + \tau\mu\|\boldsymbol{h}_b^{n+1}\|^2.$$

Proof. Taking $\boldsymbol{v} = \tilde{\boldsymbol{u}}^{n+1}$ in (4.1), we get

$$\begin{aligned}
&(\tilde{D}_t\boldsymbol{u}^{n+1}, \tilde{\boldsymbol{u}}^{n+1}) + \nu\|\nabla\tilde{\boldsymbol{u}}^{n+1}\|^2 + \nu_r\|\nabla\times\tilde{\boldsymbol{u}}^{n+1}\|^2 + \nu_r\|\nabla\cdot\tilde{\boldsymbol{u}}^{n+1}\|^2 + (\nabla p^n, \tilde{\boldsymbol{u}}^{n+1}) \\
&\quad = Q^{n+1}2\nu_r(\boldsymbol{w}^*, \nabla\times\tilde{\boldsymbol{u}}^{n+1}) \underbrace{-Q^{n+1}((\boldsymbol{u}^*\cdot\nabla)\boldsymbol{u}^*, \tilde{\boldsymbol{u}}^{n+1})}_{\text{I}} \\
&\qquad \underbrace{-Q^{n+1}\mu((\tilde{\boldsymbol{u}}^{n+1}\cdot\nabla)\boldsymbol{m}^*, \boldsymbol{h}^*)}_{\text{II}} \underbrace{-Q^{n+1}\mu((\nabla\cdot\tilde{\boldsymbol{u}}^{n+1})\boldsymbol{m}^*, \boldsymbol{h}^*)}_{\text{III}}.
\end{aligned} \tag{4.9}$$

Taking $\boldsymbol{Z} = \boldsymbol{w}^{n+1}$ in (4.4), we derive

$$\begin{aligned}
&\zeta(D_t\boldsymbol{w}^{n+1}, \boldsymbol{w}^{n+1}) + c_1\|\nabla\boldsymbol{w}^{n+1}\|^2 + c_2\|\nabla\cdot\boldsymbol{w}^{n+1}\|^2 + 4\nu_r\|\boldsymbol{w}^{n+1}\|^2 \\
&= \underbrace{Q^{n+1}2\nu_r(\nabla\times\boldsymbol{u}^*, \boldsymbol{w}^{n+1})}_{\text{IV}} \underbrace{-Q^{n+1}\zeta((\boldsymbol{u}^*\cdot\nabla)\boldsymbol{w}^*, \boldsymbol{w}^{n+1})}_{\text{V}} \underbrace{+Q^{n+1}\mu(\boldsymbol{m}^*\times\boldsymbol{h}^*, \boldsymbol{w}^{n+1})}_{\text{VI}}.
\end{aligned} \tag{4.10}$$

Taking $\psi = \mu\varphi^{n+1}$ in (4.5), we derive

(4.11)
$$\begin{aligned}\mu(\nabla D_t\varphi^{n+1},\nabla\varphi^{n+1}) &+ \frac{\mu}{\tau}\|\nabla\varphi^{n+1}\|^2 + \frac{\mu\chi_0}{\tau}\|\nabla\varphi^{n+1}\|^2\\ &= \underbrace{Q^{n+1}\mu((\boldsymbol{u}^*\cdot\nabla)\boldsymbol{m}^*,\nabla\varphi^{n+1})}_{\text{VII}}\underbrace{-Q^{n+1}\mu(\boldsymbol{w}^*\times\boldsymbol{m}^*,\nabla\varphi^{n+1})}_{\text{VIII}}\\ &\quad+\frac{\mu}{\tau}(\boldsymbol{h}_a^{n+1},\nabla\varphi^{n+1})+\mu(\boldsymbol{h}_b^{n+1},\nabla\varphi^{n+1}).\end{aligned}$$

Taking $\boldsymbol{n} = \frac{\mu}{\chi_0}\boldsymbol{m}^{n+1}$ in (4.6), we obtain

(4.12)
$$\begin{aligned}&\frac{\mu}{\chi_0}(D_t\boldsymbol{m}^{n+1},\boldsymbol{m}^{n+1}) + \frac{\mu}{\tau\chi_0}\|\boldsymbol{m}^{n+1}\|^2\\ &\quad=\underbrace{Q^{n+1}\frac{\mu}{\chi_0}(\boldsymbol{w}^*\times\boldsymbol{m}^*,\boldsymbol{m}^{n+1})}_{\text{IX}}\underbrace{-Q^{n+1}\frac{\mu}{\chi_0}((\boldsymbol{u}^*\cdot\nabla)\boldsymbol{m}^*,\boldsymbol{m}^{n+1})}_{\text{X}}+\frac{\mu}{\tau}(\boldsymbol{h}^{n+1},\boldsymbol{m}^{n+1}).\end{aligned}$$

Multiplying Q^{n+1} on (4.7), we derive

(4.13)
$$\begin{aligned}&Q^{n+1}D_tQ^{n+1} + |Q^{n+1}|^2 8\nu_r\|\boldsymbol{w}^*\|^2\\ &\quad= Q^{n+1}8\nu_r(\boldsymbol{w}^*,\boldsymbol{w}^{n+1}) + Q^{n+1}2\nu_r(\boldsymbol{w}^*,\nabla\times\tilde{\boldsymbol{u}}^{n+1})\underbrace{-Q^{n+1}2\nu_r(\nabla\times\boldsymbol{u}^*,\boldsymbol{w}^{n+1})}_{-\text{IV}}\\ &\quad\underbrace{+Q^{n+1}((\boldsymbol{u}^*\cdot\nabla)\boldsymbol{u}^*,\tilde{\boldsymbol{u}}^{n+1})}_{-\text{I}}\underbrace{+Q^{n+1}\zeta((\boldsymbol{u}^*\cdot\nabla)\boldsymbol{w}^*,\boldsymbol{w}^{n+1})}_{-\text{V}}\\ &\quad\underbrace{+Q^{n+1}\frac{\mu}{\chi_0}((\boldsymbol{u}^*\cdot\nabla)\boldsymbol{m}^*,\boldsymbol{m}^{n+1})}_{-\text{X}}\underbrace{-Q^{n+1}\frac{\mu}{\chi_0}(\boldsymbol{w}^*\times\boldsymbol{m}^*,\boldsymbol{m}^{n+1})}_{-\text{IX}}\\ &\quad\underbrace{+Q^{n+1}\mu(\boldsymbol{w}^*\times\boldsymbol{m}^*,\nabla\varphi^{n+1})}_{-\text{VIII}}\underbrace{-Q^{n+1}\mu(\boldsymbol{m}^*\times\nabla\varphi^*,\boldsymbol{w}^{n+1})}_{-\text{VI}}\\ &\quad\underbrace{+Q^{n+1}\mu((\tilde{\boldsymbol{u}}^{n+1}\cdot\nabla)\boldsymbol{m}^*,\nabla\varphi^*)}_{-\text{II}}\underbrace{-Q^{n+1}\mu((\boldsymbol{u}^*\cdot\nabla)\boldsymbol{m}^*,\nabla\varphi^{n+1})}_{-\text{VII}}\\ &\quad\underbrace{+Q^{n+1}\mu((\nabla\cdot\tilde{\boldsymbol{u}}^{n+1})\boldsymbol{m}^*,\nabla\varphi^*)}_{-\text{III}}.\end{aligned}$$

Combining (4.9)–(4.13) and cancelling out the terms labeled by the same Roman numerals, we obtain

(4.14)
$$\begin{aligned}&(\tilde{D}_t\boldsymbol{u}^{n+1},\tilde{\boldsymbol{u}}^{n+1})\\ &\quad+(\nabla p^n,\tilde{\boldsymbol{u}}^{n+1})+\nu\|\nabla\tilde{\boldsymbol{u}}^{n+1}\|^2+\nu_r\|\nabla\times\tilde{\boldsymbol{u}}^{n+1}\|^2+\nu_r\|\nabla\cdot\tilde{\boldsymbol{u}}^{n+1}\|^2\\ &\quad+\zeta(D_t\boldsymbol{w}^{n+1},\boldsymbol{w}^{n+1})+c_1\|\nabla\boldsymbol{w}^{n+1}\|^2+c_2\|\nabla\cdot\boldsymbol{w}^{n+1}\|^2+4\nu_r\|\boldsymbol{w}^{n+1}\|^2\\ &\quad+\mu(\nabla D_t\varphi^{n+1},\nabla\varphi^{n+1})+\frac{\mu}{\tau}\|\nabla\varphi^{n+1}\|^2+\frac{\mu\chi_0}{\tau}\|\nabla\varphi^{n+1}\|^2+\frac{\mu}{\chi_0}(D_t\boldsymbol{m}^{n+1},\boldsymbol{m}^{n+1})\\ &\quad+\frac{\mu}{\tau\chi_0}\|\boldsymbol{m}^{n+1}\|^2+Q^{n+1}D_tQ^{n+1}+|Q^{n+1}|^28\nu_r\|\boldsymbol{w}^*\|^2\\ &\quad=\frac{\mu}{\tau}(\boldsymbol{h}_a^{n+1},\boldsymbol{h}^{n+1})+\mu(\boldsymbol{h}_b^{n+1},\boldsymbol{h}^{n+1})+\frac{\mu}{\tau}(\boldsymbol{h}^{n+1},\boldsymbol{m}^{n+1})\\ &\quad+Q^{n+1}4\nu_r(\boldsymbol{w}^*,\nabla\times\tilde{\boldsymbol{u}}^{n+1})+Q^{n+1}8\nu_r(\boldsymbol{w}^*,\boldsymbol{w}^{n+1}).\end{aligned}$$

From (4.3), we derive the orthogonal identity: for $\boldsymbol{v} \in \boldsymbol{H} = \{\boldsymbol{v} \in \boldsymbol{L}^2(\Omega) : (\boldsymbol{v}, \nabla q) = 0 \ \forall q \in Q_h\}$,

$$(\boldsymbol{u}^{n+1} - \tilde{\boldsymbol{u}}^{n+1}, \boldsymbol{v}) = \frac{2\delta t}{3}(\nabla p^n - \nabla p^{n+1}, \boldsymbol{v}) = 0. \tag{4.15}$$

Using (4.15) and (4.8), we have

$$\begin{aligned}(\tilde{D}_t \boldsymbol{u}^{n+1}, \tilde{\boldsymbol{u}}^{n+1}) &= \frac{1}{2\delta t}(3\boldsymbol{u}^{n+1} - 4\boldsymbol{u}^n + \boldsymbol{u}^{n-1}, \tilde{\boldsymbol{u}}^{n+1}) + \frac{1}{2\delta t}(3\tilde{\boldsymbol{u}}^{n+1} - 3\boldsymbol{u}^{n+1}, \tilde{\boldsymbol{u}}^{n+1}) \\ &= \frac{1}{2\delta t}(3\boldsymbol{u}^{n+1} - 4\boldsymbol{u}^n + \boldsymbol{u}^{n-1}, \boldsymbol{u}^{n+1}) + \frac{1}{2\delta t}(3\tilde{\boldsymbol{u}}^{n+1} - 3\boldsymbol{u}^{n+1}, \tilde{\boldsymbol{u}}^{n+1} - \boldsymbol{u}^{n+1}) \\ &= \frac{1}{4\delta t}(\|\boldsymbol{u}^{n+1}\|^2 - \|\boldsymbol{u}^n\|^2 + \|2\boldsymbol{u}^{n+1} - \boldsymbol{u}^n\|^2 - \|2\boldsymbol{u}^n - \boldsymbol{u}^{n-1}\|^2 + \|\boldsymbol{u}^{n+1} - \boldsymbol{u}^*\|^2) \\ &\quad + \frac{3}{2\delta t}\|\tilde{\boldsymbol{u}}^{n+1} - \boldsymbol{u}^{n+1}\|^2,\end{aligned} \tag{4.16}$$

where we use the following identity:

$$(3a - 4b + c, 2a) = a^2 - b^2 + (2a - b)^2 - (2b - c)^2 + (a - 2b + c)^2. \tag{4.17}$$

We rewrite (4.3) as

$$\boldsymbol{u}^{n+1} + \frac{2}{3}\delta t \nabla p^{n+1} = \tilde{\boldsymbol{u}}^{n+1} + \frac{2}{3}\delta t \nabla p^n.$$

By taking the L^2 inner product of the above equation with itself and using (4.8), we derive

$$\begin{aligned}(\tilde{\boldsymbol{u}}^{n+1}, \nabla p^n) &= \frac{3}{4\delta t}\|\boldsymbol{u}^{n+1}\|^2 - \frac{3}{4\delta t}\|\tilde{\boldsymbol{u}}^{n+1}\|^2 + \frac{\delta t}{3}\|\nabla p^{n+1}\|^2 - \frac{\delta t}{3}\|\nabla p^n\|^2 \\ &= -\frac{3}{4\delta t}\|\boldsymbol{u}^{n+1} - \tilde{\boldsymbol{u}}^{n+1}\|^2 + \frac{\delta t}{3}\|\nabla p^{n+1}\|^2 - \frac{\delta t}{3}\|\nabla p^n\|^2,\end{aligned} \tag{4.18}$$

where we also utilize (4.15). Combining (4.16) with (4.18), we obtain

$$\begin{aligned}(\tilde{D}_t \boldsymbol{u}^{n+1}, \tilde{\boldsymbol{u}}^{n+1}) + (\nabla p^n, \tilde{\boldsymbol{u}}^{n+1}) &= \frac{3}{4\delta t}\|\boldsymbol{u}^{n+1} - \tilde{\boldsymbol{u}}^{n+1}\|^2 + \frac{\delta t}{3}\|\nabla p^{n+1}\|^2 - \frac{\delta t}{3}\|\nabla p^n\|^2 \\ &\quad + \frac{1}{4\delta t}(\|\boldsymbol{u}^{n+1}\|^2 - \|\boldsymbol{u}^n\|^2 + \|2\boldsymbol{u}^{n+1} - \boldsymbol{u}^n\|^2 - \|2\boldsymbol{u}^n - \boldsymbol{u}^{n-1}\|^2 + \|\boldsymbol{u}^{n+1} - \boldsymbol{u}^*\|^2).\end{aligned} \tag{4.19}$$

By using the Cauchy–Schwarz inequality, we further estimate the terms on the right-hand side of (4.14) as follows:

$$\begin{cases}\dfrac{\mu}{\tau}(\boldsymbol{h}_a^{n+1}, \boldsymbol{h}^{n+1}) + \mu(\boldsymbol{h}_b^{n+1}, \boldsymbol{h}^{n+1}) + \dfrac{\mu}{\tau}(\boldsymbol{h}^{n+1}, \boldsymbol{m}^{n+1}) \\ \quad \le \dfrac{\mu}{2\tau}\|\boldsymbol{h}^{n+1}\|^2 + \dfrac{\mu}{\tau}\|\boldsymbol{h}_a^{n+1}\|^2 + \tau\mu\|\boldsymbol{h}_b^{n+1}\|^2 + \dfrac{\mu}{4\tau\chi_0}\|\boldsymbol{m}^{n+1}\|^2 + \dfrac{\chi_0\mu}{\tau}\|\boldsymbol{h}^{n+1}\|^2, \\ Q^{n+1} 4\nu_r(\boldsymbol{w}^*, \nabla\times\tilde{\boldsymbol{u}}^{n+1}) \le |Q^{n+1}| 4\nu_r \|\boldsymbol{w}^*\| \|\nabla\times\tilde{\boldsymbol{u}}^{n+1}\| \le \nu_r \|\nabla\times\tilde{\boldsymbol{u}}^{n+1}\|^2 \\ \quad + |Q^{n+1}|^2 4\nu_r \|\boldsymbol{w}^*\|^2, \\ Q^{n+1} 8\nu_r(\boldsymbol{w}^*, \boldsymbol{w}^{n+1}) \le |Q^{n+1}| 8\nu_r \|\boldsymbol{w}^*\| \|\boldsymbol{w}^{n+1}\| \le 4\nu_r \|\boldsymbol{w}^{n+1}\|^2 + |Q^{n+1}|^2 4\nu_r \|\boldsymbol{w}^*\|^2.\end{cases} \tag{4.20}$$

Finally, by combining (4.14) with (4.19)–(4.20), using (4.17), and dropping some unnecessary terms, we obtain

$$\begin{aligned}
&\frac{1}{4\delta t}(\|\boldsymbol{u}^{n+1}\|^2-\|\boldsymbol{u}^n\|^2+\|2\boldsymbol{u}^{n+1}-\boldsymbol{u}^n\|^2-\|2\boldsymbol{u}^n-\boldsymbol{u}^{n-1}\|^2)+\frac{\delta t}{3}\|\nabla p^{n+1}\|^2\\
&\quad-\frac{\delta t}{3}\|\nabla p^n\|^2+\frac{\zeta}{4\delta t}(\|\boldsymbol{w}^{n+1}\|^2-\|\boldsymbol{w}^n\|^2+\|2\boldsymbol{w}^{n+1}-\boldsymbol{w}^n\|^2-\|2\boldsymbol{w}^n-\boldsymbol{w}^{n-1}\|^2)\\
&\quad+\frac{\mu}{4\delta t}(\|\boldsymbol{h}^{n+1}\|^2-\|\boldsymbol{h}^n\|^2+\|2\boldsymbol{h}^{n+1}-\boldsymbol{h}^n\|^2-\|2\boldsymbol{h}^n-\boldsymbol{h}^{n-1}\|^2)\\
&\quad+\frac{\mu}{\chi_0}\frac{1}{4\delta t}(\|\boldsymbol{m}^{n+1}\|^2-\|\boldsymbol{m}^n\|^2+\|2\boldsymbol{m}^{n+1}-\boldsymbol{m}^n\|^2-\|2\boldsymbol{m}^n-\boldsymbol{m}^{n-1}\|^2)\\
&\quad+\frac{1}{4\delta t}(|Q^{n+1}|^2-|Q^n|^2+|2Q^{n+1}-Q^n|^2-|2Q^n-Q^{n-1}|^2)\\
&\qquad+\nu\|\nabla\tilde{\boldsymbol{u}}^{n+1}\|^2+\nu_r\|\nabla\cdot\tilde{\boldsymbol{u}}^{n+1}\|^2\\
&\quad+c_1\|\nabla\boldsymbol{w}^{n+1}\|^2+c_2\|\nabla\cdot\boldsymbol{w}^{n+1}\|^2+\frac{\mu}{2\tau}\|\boldsymbol{h}^{n+1}\|^2+\frac{3\mu}{4\tau\chi_0}\|\boldsymbol{m}^{n+1}\|^2\\
&\quad\le\frac{\mu}{\tau}\|\boldsymbol{h}_a^{n+1}\|^2+\tau\mu\|\boldsymbol{h}_b^{n+1}\|^2.
\end{aligned}$$

The proof is completed. ∎

4.2. Decoupled implementation. Formally, the scheme (4.1)–(4.7) is an unknowns-Q coupled algorithm, but thanks to scalar property of Q, it can achieve a fully decoupled manner by splitting the unknowns in terms of Q, as discussed below.

We split the unknowns $\tilde{\boldsymbol{u}}^{n+1}$, $\boldsymbol{w}^{n+1}$, φ^{n+1}, $\boldsymbol{m}^{n+1}$ into the following form:

$$\begin{aligned}
&\tilde{\boldsymbol{u}}^{n+1}=\tilde{\boldsymbol{u}}_a^{n+1}+Q^{n+1}\tilde{\boldsymbol{u}}_b^{n+1},\ \boldsymbol{w}^{n+1}=\boldsymbol{w}_a^{n+1}+Q^{n+1}\boldsymbol{w}_b^{n+1},\\
&\varphi^{n+1}=\varphi_a^{n+1}+Q^{n+1}\varphi_b^{n+1},\ \boldsymbol{m}^{n+1}=\boldsymbol{m}_a^{n+1}+Q^{n+1}\boldsymbol{m}_b^{n+1},
\end{aligned}\tag{4.21}$$

for $\tilde{\boldsymbol{u}}_k^{n+1}\in\boldsymbol{V}_h$, $\boldsymbol{w}_k^{n+1}\in\boldsymbol{\mathcal{Z}}_h$, $\varphi_k^{n+1}\in\Psi_h$, and $\boldsymbol{m}_k^{n+1}\in\boldsymbol{N}_h$, $k=a,b$.

Step 1. Using the split form in (4.21) and and applying the nonlocal feature of Q^{n+1}, we split (4.1) into the following two subequations: find $\tilde{\boldsymbol{u}}_a^{n+1},\tilde{\boldsymbol{u}}_b^{n+1}\in\boldsymbol{V}_h$, such that for all $\boldsymbol{v}\in\boldsymbol{V}_h$, there hold

$$\begin{cases}
\dfrac{3}{2\delta t}(\tilde{\boldsymbol{u}}_a^{n+1},\boldsymbol{v})+\nu(\nabla\tilde{\boldsymbol{u}}_a^{n+1},\nabla\boldsymbol{v})+\nu_r(\nabla\times\tilde{\boldsymbol{u}}_a^{n+1},\nabla\times\boldsymbol{v})+\nu_r(\nabla\cdot\tilde{\boldsymbol{u}}_a^{n+1},\nabla\cdot\boldsymbol{v})\\
c=\dfrac{1}{2\delta t}(4\boldsymbol{u}^n-\boldsymbol{u}^{n-1},\boldsymbol{v})-(\nabla p^n,\boldsymbol{v}),\\
\dfrac{3}{2\delta t}(\tilde{\boldsymbol{u}}_b^{n+1},\boldsymbol{v})+\nu(\nabla\tilde{\boldsymbol{u}}_b^{n+1},\nabla\boldsymbol{v})+\nu_r(\nabla\times\tilde{\boldsymbol{u}}_b^{n+1},\nabla\times\boldsymbol{v})+\nu_r(\nabla\cdot\tilde{\boldsymbol{u}}_b^{n+1},\nabla\cdot\boldsymbol{v})\\
=2\nu_r(\boldsymbol{w}^*,\nabla\times\boldsymbol{v})-\mu((\boldsymbol{v}\cdot\nabla)\boldsymbol{m}^*,\nabla\varphi^*)-\mu((\nabla\cdot\boldsymbol{v})\boldsymbol{m}^*,\nabla\varphi^*)-(\boldsymbol{u}^*\cdot\nabla)\boldsymbol{u}^*,\boldsymbol{v}).
\end{cases}\tag{4.22}$$

Step 2. Using the split form in (4.21), we split (4.4) into two subequations as follows: find $\boldsymbol{w}_a^{n+1},\boldsymbol{w}_b^{n+1}\in\boldsymbol{\mathcal{Z}_h}$, such that for all $\boldsymbol{Z}\in\boldsymbol{\mathcal{Z}_h}$, there hold

$$\begin{cases}
\dfrac{3\zeta}{2\delta t}(\boldsymbol{w}_a^{n+1},\boldsymbol{Z})+c_1(\nabla\boldsymbol{w}_a^{n+1},\nabla\boldsymbol{Z})+c_2(\nabla\cdot\boldsymbol{w}_a^{n+1},\nabla\cdot\boldsymbol{Z})+4\nu_r(\boldsymbol{w}_a^{n+1},\boldsymbol{Z})\\
\qquad=\dfrac{\zeta}{2\delta t}(4\boldsymbol{w}^n-\boldsymbol{w}^{n-1},\boldsymbol{Z}),\\
\dfrac{3\zeta}{2\delta t}(\boldsymbol{w}_b^{n+1},\boldsymbol{Z})+c_1(\nabla\boldsymbol{w}_b^{n+1},\nabla\boldsymbol{Z})+c_2(\nabla\cdot\boldsymbol{w}_b^{n+1},\nabla\cdot\boldsymbol{Z})+4\nu_r(\boldsymbol{w}_b^{n+1},\boldsymbol{Z})\\
\qquad=2\nu_r(\nabla\times\boldsymbol{u}^*,\boldsymbol{Z})+\mu(\boldsymbol{m}^*\times\nabla\varphi^*,\boldsymbol{Z})-\zeta((\boldsymbol{u}^*\cdot\nabla)\boldsymbol{w}^*,\boldsymbol{Z}).
\end{cases}\tag{4.23}$$

Step 3. Using the split form in (4.21), we split (4.5) into two subequations as follows: find $\varphi_a^{n+1}, \varphi_b^{n+1} \in \Psi_h$, such that for all $\psi \in \Psi_h$, there hold

(4.24)
$$\begin{cases} \dfrac{3}{2\delta t}(\nabla\varphi_a^{n+1}, \nabla\psi) + \dfrac{1}{\tau}(\nabla\varphi_a^{n+1}, \nabla\psi) + \dfrac{\chi_0}{\tau}(\nabla\varphi_a^{n+1}, \nabla\psi) \\ \qquad = \dfrac{1}{2\delta t}(4\nabla\varphi^n - \nabla\varphi^{n-1}, \nabla\psi) + \dfrac{1}{\tau}(\boldsymbol{h}_a^{n+1}, \nabla\psi) + (\boldsymbol{h}_b^{n+1}, \nabla\psi), \\ \dfrac{3}{2\delta t}(\nabla\varphi_b^{n+1}, \nabla\psi) + \dfrac{1}{\tau}(\nabla\varphi_b^{n+1}, \nabla\psi) + \dfrac{\chi_0}{\tau}(\nabla\varphi_b^{n+1}, \nabla\psi) \\ \qquad = ((\boldsymbol{u}^* \cdot \nabla)\boldsymbol{m}^*, \nabla\psi) - (\boldsymbol{w}^* \times \boldsymbol{m}^*, \nabla\psi). \end{cases}$$

Step 4. Using the split form in (4.21), we split (4.6) into two subequations as follows: find $\boldsymbol{m}_a^{n+1}$, $\boldsymbol{m}_b^{n+1} \in \boldsymbol{N}_h$, such that for all $\boldsymbol{n} \in \boldsymbol{N}_h$, there hold

(4.25)
$$\begin{cases} \dfrac{3}{2\delta t}(\boldsymbol{m}_a^{n+1}, \boldsymbol{n}) + \dfrac{1}{\tau}(\boldsymbol{m}_a^{n+1}, \boldsymbol{n}) = \dfrac{1}{2\delta t}(4\boldsymbol{m}^n - \boldsymbol{m}^{n-1}, \boldsymbol{n}) + \dfrac{\chi_0}{\tau}(\nabla\varphi_a^{n+1}, \boldsymbol{n}), \\ \dfrac{3}{2\delta t}(\boldsymbol{m}_b^{n+1}, \boldsymbol{n}) + \dfrac{1}{\tau}(\boldsymbol{m}_b^{n+1}, \boldsymbol{n}) = (\boldsymbol{w}^* \times \boldsymbol{m}^*, \boldsymbol{n}) - ((\boldsymbol{u}^* \cdot \nabla)\boldsymbol{m}^*, \boldsymbol{n}) + \dfrac{\chi_0}{\tau}(\nabla\varphi_b^{n+1}, \boldsymbol{n}). \end{cases}$$

Step 5. To solve Q^{n+1}, we use the split form of (4.21) in (4.7) and rewrite (4.7) s the following form:

$$\Big(\frac{3}{2\delta t} + 8\nu_r\|\boldsymbol{w}^*\|^2 - \eta_b\Big)Q^{n+1} = \frac{1}{2\delta t}(4Q^n - Q^{n-1}) + \eta_a, \tag{4.26}$$

where for $i = a,\ b$,

(4.27)
$$\begin{aligned} \eta_i = {} & 8\nu_r(\boldsymbol{w}^*, \boldsymbol{w}_i^{n+1}) \underbrace{+2\nu_r(\boldsymbol{w}^*, \nabla\times\tilde{\boldsymbol{u}}_i^{n+1})}_{T_1} \underbrace{-2\nu_r(\nabla\times\boldsymbol{u}^*, \boldsymbol{w}_i^{n+1})}_{T_2} \underbrace{+((\boldsymbol{u}^*\cdot\nabla)\boldsymbol{u}^*, \tilde{\boldsymbol{u}}_i^{n+1})}_{T_3} \\ & \underbrace{+\zeta((\boldsymbol{u}^*\cdot\nabla)\boldsymbol{w}^*, \boldsymbol{w}_i^{n+1})}_{T_4} \underbrace{+\frac{\mu}{\chi_0}((\boldsymbol{u}^*\cdot\nabla)\boldsymbol{m}^*, \boldsymbol{m}_i^{n+1})}_{T_5} \underbrace{-\frac{\mu}{\chi_0}(\boldsymbol{w}^*\times\boldsymbol{m}^*, \boldsymbol{m}_i^{n+1})}_{T_6} \\ & \underbrace{+\mu(\boldsymbol{w}^*\times\boldsymbol{m}^*, \nabla\varphi_i^{n+1})}_{T_7} \underbrace{-\mu(\boldsymbol{m}^*\times\nabla\varphi^*, \boldsymbol{w}_i^{n+1})}_{T_8} \\ & \underbrace{+\mu((\tilde{\boldsymbol{u}}_i^{n+1}\cdot\nabla)\boldsymbol{m}^*, \nabla\varphi^*)}_{T_9} \underbrace{-\mu((\boldsymbol{u}^*\cdot\nabla)\boldsymbol{m}^*, \nabla\varphi_i^{n+1})}_{T_{10}} \underbrace{+\mu((\nabla\cdot\tilde{\boldsymbol{u}}_i^{n+1})\boldsymbol{m}^*, \nabla\varphi^*)}_{T_{11}}. \end{aligned}$$

Step 6. After completing Steps 1–5, we update $\tilde{\boldsymbol{u}}^{n+1}$, $\boldsymbol{w}^{n+1}$, φ^{n+1}, $\boldsymbol{m}^{n+1}$ by using the split form (4.21); then we update p^{n+1} by (4.2); we update $\boldsymbol{u}^{n+1}$ by (4.3).

From Steps 1–6, it is evident that the scheme possesses a fully decoupled structure. Meanwhile, it is also a linear, time-second-order accurate, and unconditionally energy-stable scheme. Moreover, the implementation of this scheme demands only a few independent linear elliptic/parabolic problems with constant coefficients to be solved. The final task is to demonstrate the unique solvability of the equations outlined in Steps 1–6.

THEOREM 4.2. *The equations in* (4.22)–(4.26) *and* (4.2) *are uniquely solvable.*

Proof. The well-posedness of problems (4.22)–(4.25) and (4.2) in Steps 1–4 and Step 6 could be proved by the Lax–Milgram theorem [4], where equations (4.25) also need inverse inequality [4]. Because the related proofs refer to standard argument, we omit the details here.

We show the unique solvability of (4.26) as follows. Taking $\boldsymbol{v} = \tilde{\boldsymbol{u}}_b^{n+1}$ in the second equation of (4.22), we derive

$$
\begin{aligned}
(A1 :=)\ & \underbrace{-2\nu_r(\boldsymbol{w}^*, \nabla\times \tilde{\boldsymbol{u}}_b^{n+1})}_{-T_1}\underbrace{-((\boldsymbol{u}^*\cdot\nabla)\boldsymbol{u}^*, \tilde{\boldsymbol{u}}_b^{n+1})}_{-T_3} \\
& \underbrace{-\mu((\tilde{\boldsymbol{u}}_b^{n+1}\cdot\nabla)\boldsymbol{m}^*, \nabla\varphi^*)}_{-T_9}\underbrace{-\mu((\nabla\cdot\tilde{\boldsymbol{u}}_b^{n+1})\boldsymbol{m}^*, \nabla\varphi^*)}_{-T_{11}} \\
& = \frac{3}{2\delta t}\|\tilde{\boldsymbol{u}}_b^{n+1}\|^2 + \nu\|\nabla\tilde{\boldsymbol{u}}_b^{n+1}\|^2 + \nu_r\|\nabla\times\tilde{\boldsymbol{u}}_b^{n+1}\|^2 + \nu_r\|\nabla\cdot\tilde{\boldsymbol{u}}_b^{n+1}\|^2 \\
& \quad - 4\nu_r(\boldsymbol{w}^*, \nabla\times\tilde{\boldsymbol{u}}_b^{n+1}).
\end{aligned}
\tag{4.28}
$$

Taking $\boldsymbol{Z} = \boldsymbol{w}_b^{n+1}$ in the second equation of (4.23), we obtain

$$
\begin{aligned}
(A_2 :=)\ & \underbrace{2\nu_r(\nabla\times\boldsymbol{u}^*, \boldsymbol{w}_b^{n+1})}_{-T_2}\underbrace{-\zeta((\boldsymbol{u}^*\cdot\nabla)\boldsymbol{w}^*, \boldsymbol{w}_b^{n+1})}_{-T_4}\underbrace{+\mu(\boldsymbol{m}^*\times\nabla\varphi^*, \boldsymbol{w}_b^{n+1})}_{-T_8} \\
& = \frac{3\zeta}{2\delta t}\|\boldsymbol{w}_b^{n+1}\|^2 + c_1\|\nabla\boldsymbol{w}_b^{n+1}\|^2 + c_2\|\nabla\cdot\boldsymbol{w}_b^{n+1}\|^2 + 4\nu_r\|\boldsymbol{w}_b^{n+1}\|^2.
\end{aligned}
\tag{4.29}
$$

Taking $\psi = \mu\varphi_b^{n+1}$ in the second equation of (4.24), we get

$$
\begin{aligned}
(A_3 :=)\ & \underbrace{\mu((\boldsymbol{u}^*\cdot\nabla)\boldsymbol{m}^*, \nabla\varphi_b^{n+1})}_{-T_{10}}\underbrace{-\mu(\boldsymbol{w}^*\times\boldsymbol{m}^*, \nabla\varphi_b^{n+1})}_{-T_7} \\
& = \frac{3\mu}{2\delta t}\|\nabla\varphi_b^{n+1}\|^2 + \frac{\mu}{\tau}\|\nabla\varphi_b^{n+1}\|^2 + \frac{\mu\chi_0}{\tau}\|\nabla\varphi_b^{n+1}\|^2.
\end{aligned}
\tag{4.30}
$$

Taking $\boldsymbol{n} = \frac{\mu}{\chi_0}\boldsymbol{m}_b^{n+1}$ in the second equation of (4.25), there holds

$$
\begin{aligned}
(A_4 :=)\ & \underbrace{\frac{\mu}{\chi_0}(\boldsymbol{w}^*\times\boldsymbol{m}^*, \boldsymbol{m}_b^{n+1})}_{-T_6}\underbrace{-\frac{\mu}{\chi_0}((\boldsymbol{u}^*\cdot\nabla)\boldsymbol{m}^*, \boldsymbol{m}_b^{n+1})}_{-T_5} \\
& = \frac{3\mu}{2\delta t\chi_0}\|\boldsymbol{m}_b^{n+1}\|^2 + \frac{\mu}{\chi_0\tau}\|\boldsymbol{m}_b^{n+1}\|^2 - \frac{\mu}{\tau}(\nabla\varphi_b^{n+1}, \boldsymbol{m}_b^{n+1}).
\end{aligned}
\tag{4.31}
$$

From (4.27), it is easy to see that $\eta_b = -A_1 - A_2 - A_3 - A_4 + 8\nu_r(\boldsymbol{w}^*, \boldsymbol{w}_b^{n+1})$. Hence, using (4.28)–(4.31), we derive

$$
\begin{aligned}
& 8\nu_r\|\boldsymbol{w}^*\|^2 - \eta_b = 8\nu_r\|\boldsymbol{w}^*\|^2 + A_1 + A_2 + A_3 + A_4 - 8\nu_r(\boldsymbol{w}^*, \boldsymbol{w}_b^{n+1}) \\
& = 8\nu_r\|\boldsymbol{w}^*\|^2 + \frac{3}{2\delta t}\|\tilde{\boldsymbol{u}}_b^{n+1}\|^2 + \nu\|\nabla\tilde{\boldsymbol{u}}_b^{n+1}\|^2 + \nu_r\|\nabla\times\tilde{\boldsymbol{u}}_b^{n+1}\|^2 + \nu_r\|\nabla\cdot\tilde{\boldsymbol{u}}_b^{n+1}\|^2 \\
& \quad + \frac{3\zeta}{2\delta t}\|\boldsymbol{w}_b^{n+1}\|^2 + c_1\|\nabla\boldsymbol{w}_b^{n+1}\|^2 + c_2\|\nabla\cdot\boldsymbol{w}_b^{n+1}\|^2 + 4\nu_r\|\boldsymbol{w}_b^{n+1}\|^2 + \frac{3\mu}{2\delta t}\|\nabla\varphi_b^{n+1}\|^2 \\
& \quad + \frac{\mu}{\tau}\|\nabla\varphi_b^{n+1}\|^2 + \frac{\mu\chi_0}{\tau}\|\nabla\varphi_b^{n+1}\|^2 + \frac{3\mu}{2\delta t\chi_0}\|\boldsymbol{m}_b^{n+1}\|^2 + \frac{\mu}{\chi_0\tau}\|\boldsymbol{m}_b^{n+1}\|^2 \\
& \quad - 4\nu_r(\boldsymbol{w}^*, \nabla\times\tilde{\boldsymbol{u}}_b^{n+1}) - \frac{\mu}{\tau}(\nabla\varphi_b^{n+1}, \boldsymbol{m}_b^{n+1}) - 8\nu_r(\boldsymbol{w}^*, \boldsymbol{w}_b^{n+1}).
\end{aligned}
\tag{4.32}
$$

Using the Cauchy–Schwarz inequality, we derive the following estimates:

(4.33)
$$\begin{cases} 8\nu_r|(\boldsymbol{w}^*,\boldsymbol{w}_b^{n+1})| \le 8\nu_r\|\boldsymbol{w}^*\|\|\boldsymbol{w}_b^{n+1}\| \le 4\nu_r\|\boldsymbol{w}^*\|^2 + 4\nu_r\|\boldsymbol{w}_b^{n+1}\|^2, \\ 4\nu_r|(\boldsymbol{w}^*,\nabla\times\tilde{\boldsymbol{u}}_b^{n+1})| \le 4\nu_r\|\boldsymbol{w}^*\|\|\nabla\times\tilde{\boldsymbol{u}}_b^{n+1}\| \le \nu_r\|\nabla\times\tilde{\boldsymbol{u}}_b^{n+1}\|^2 + 4\nu_r\|\boldsymbol{w}^*\|^2, \\ \dfrac{\mu}{\tau}|(\nabla\varphi_b^{n+1},\boldsymbol{m}_b^{n+1})| \le \dfrac{\mu}{\tau}\|\nabla\varphi_b^{n+1}\|\|\boldsymbol{m}_b^{n+1}\| \le \dfrac{\mu}{4\tau\chi_0}\|\boldsymbol{m}_b^{n+1}\|^2 + \dfrac{\chi_0\mu}{\tau}\|\nabla\varphi_b^{n+1}\|^2. \end{cases}$$

Combining (4.32) with (4.33), we deduce

$$\begin{aligned} 8\nu_r\|\boldsymbol{w}^*\|^2 - \eta_b \ge{}& \frac{3}{2\delta t}\|\tilde{\boldsymbol{u}}_b^{n+1}\|^2 + \nu\|\nabla\tilde{\boldsymbol{u}}_b^{n+1}\|^2 + \nu_r\|\nabla\cdot\tilde{\boldsymbol{u}}_b^{n+1}\|^2 + \frac{3\zeta}{2\delta t}\|\boldsymbol{w}_b^{n+1}\|^2 \\ &+ c_1\|\nabla\boldsymbol{w}_b^{n+1}\|^2 + c_2\|\nabla\cdot\boldsymbol{w}_b^{n+1}\|^2 + \frac{3\mu}{2\delta t}\|\nabla\varphi_b^{n+1}\|^2 + \frac{\mu}{\tau}\|\nabla\varphi_b^{n+1}\|^2 \\ &+ \frac{3\mu}{2\delta t\chi_0}\|\boldsymbol{m}_b^{n+1}\|^2 + \frac{3\mu}{4\chi_0\tau}\|\boldsymbol{m}_b^{n+1}\|^2 \ge 0. \end{aligned}$$

Thus, we obtain $\frac{3}{2\delta t} + 8\nu_r\|\boldsymbol{w}^*\|^2 - \eta_b \ne 0$, which implies the solvability of (4.26). The proof is completed. ∎

5. Numerical simulations. In this section, we carry out several numerical 2D/3D simulations to verify the accuracy and stability of our scheme. We also exhibit some intriguing phenomena related to ferrofluid rotational flow problems, specifically the spin-up flow and annular gap flow that occur when subjected to rotating magnetic fields. The study of nonmechanically driven flows is a relatively unexplored area in the physics of fluids, with promising potential for technological applications in various scenarios such as space, ocean, and biological environments.

The applied magnetic field $\boldsymbol{h}_a$ is generated by a linear combination of dipoles that reads as [13]

$$\boldsymbol{h}_a = \sum_s \alpha_s \nabla\phi_s(\boldsymbol{x}),\ \ \phi_s(\boldsymbol{x}) = \frac{\boldsymbol{d}_s\cdot(\boldsymbol{x}_s-\boldsymbol{x})}{|\boldsymbol{x}_s-\boldsymbol{x}|^d}, d=2,3, \tag{5.1}$$

where α_s denotes intensity, $|\boldsymbol{d}_s| = 1$ indicates the direction of the dipole, and $\boldsymbol{x}_s$ is the dipole's position. It is easy to verify that $\boldsymbol{h}_a$ is a harmonic field (i.e., $\nabla\times\boldsymbol{h}_a = \boldsymbol{0}$, $\nabla\cdot\boldsymbol{h}_a = 0$); cf. [20]. The first-order (linear) polynomials are used for Q_h, $\boldsymbol{\mathcal{Z}}_h$, $\boldsymbol{N}_h$, and the second-order (quadratic) polynomials are used for $\boldsymbol{V}_h$ and Ψ_h. We denote $e_w = w(t_n,\boldsymbol{x}) - w^n$, which is the approximation error at $t = t_n$, and "$a \lesssim b$" means $a \le Cb$ for some constant C.

From the chosen finite elements, the optimal error orders of the scheme (4.1)–(4.7) are expected to be

(5.2)
$$\|e_{\boldsymbol{u}}\| \lesssim \delta t^2 + h^3, \|e_{\boldsymbol{w}}\| \lesssim \delta t^2 + h^2, \|e_{\boldsymbol{h}}\| \lesssim \delta t^2 + h^2, \|e_{\boldsymbol{m}}\| \lesssim \delta t^2 + h^2, \|e_{\boldsymbol{w}}\|_1 \lesssim \delta t^2 + h,$$

Note that the L^2 error of p and the H^1 error of $\boldsymbol{u}$ are not fully second-order accurate due to the artificial Neumann boundary condition imposed on the pressure; cf. [32].

5.1. Accuracy tests. In this first numerical example, we verify the accuracy of the proposed scheme (4.1)–(4.7). We set the computational domain as $\Omega = [0,1]^2$. By imposing some appropriate force functions, we assume the FHD system (2.1)–(2.7) has the following exact solution:

$$\begin{cases} \boldsymbol{u} = (\sin(t)\sin(\pi x)\sin(\pi(y+0.5)), \sin(t)\cos(\pi x)\cos(\pi(y+0.5))), \\ \quad p = \sin(t)(2x-1)(2y-1), \\ w = \sin(2\pi x + t)\sin(2\pi y + t), \quad \varphi = (x-0.5)y\sin(t), \quad \boldsymbol{m} = (\sin(t+y), \sin(t+x)). \end{cases}$$

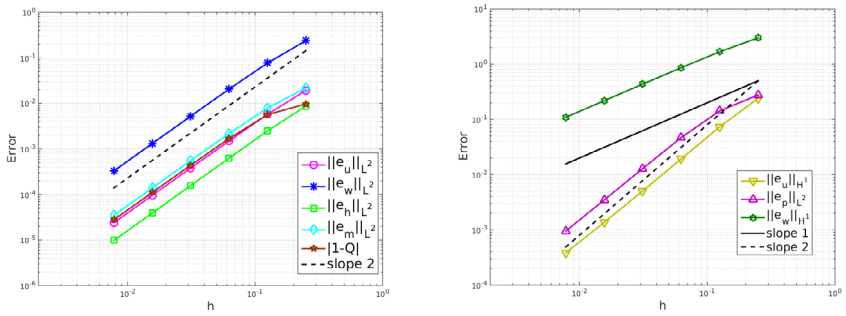

FIG. 5.1. *Numerical errors computed by fixing* $\delta t = \frac{1}{2}h$*, where (left)* $\|e_{\boldsymbol{u}}\|$*,* $\|e_w\|$*,* $\|e_{\boldsymbol{h}}\|$*,* $\|e_{\boldsymbol{m}}\|$*, and* $|1\text{-}Q|$*, and (right)* $\|e_{\boldsymbol{u}}\|_1$*,* $\|e_p\|$*, and* $\|e_w\|_1$ *are shown.*

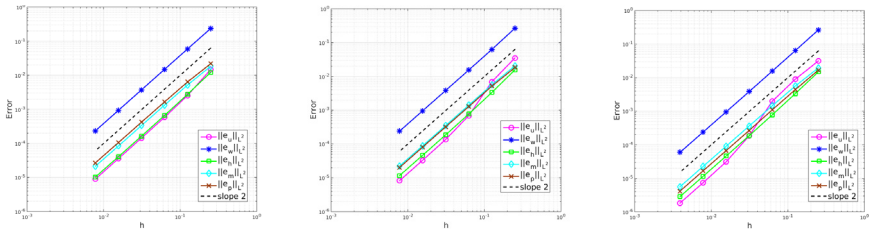

FIG. 5.2. *Numerical errors for* $\nu = \nu_r = c_1 = 0.01$ *with* $\delta t = \frac{1}{2}h$ *(left),* $\nu = \nu_r = c_1 = 0.001$ *with* $\delta t = \frac{1}{2}h$ *(middle), and* $\nu = \nu_r = c_1 = 0.0002$ *with* $\delta t = \frac{1}{4}h$ *(right).*

The model parameters are set as $\nu = \nu_r = \mu = \zeta = c_1 = \chi_0 = 1, \tau = 0.1$. To observe the convergence orders, we refine δt and h together by fixing $\delta t = \frac{1}{2}h$. With this relation, in terms of h, the expected optimal convergence orders (5.2) turns out to be

$$\|e_{\boldsymbol{u}}\| \lesssim h^2, \|e_{\boldsymbol{w}}\| \lesssim h^2, \|e_{\boldsymbol{h}}\| \lesssim h^2, \|e_{\boldsymbol{m}}\| \lesssim h^2, \|e_{\boldsymbol{w}}\|_1 \lesssim h. \tag{5.3}$$

In Figure 5.1, we plot the computed numerical errors at $t = 1$. It can be observed that the L^2 errors of $\boldsymbol{u}$, $\boldsymbol{w}$, $\boldsymbol{h}$, $\boldsymbol{m}$, and $|1\text{-}Q|$ all achieve second-order accuracy, and the H^1 error of $\boldsymbol{w}$ reaches first-order accuracy, consistent with the expected optimal orders stated in (5.3). The L^2 error of p and H^1 error of $\boldsymbol{u}$ exhibit accuracy beyond first order, but they do not achieve second-order accuracy due to an artificial Neumann boundary condition for p.

We fix $\mu = \zeta = \chi_0 = 1, \tau = 0.1$, and vary the diffusion coefficients ν, ν_r, and c_1 to test the convergence of the proposed scheme (4.1)–(4.7) under low diffusion situations. Figure 5.2 shows that for $\nu = \nu_r = c_1 = 0.01$ and $\nu = \nu_r = c_1 = 0.001$, by setting $\delta t = \frac{1}{2}h$, scheme (4.1)–(4.7) has second-order accuracy. And for $\nu = \nu_r = c_1 = 0.0002$, using the relation of $\delta t = \frac{1}{4}h$, it also preserves the second-order convergence.

Because we reformulate the magnetostatic equation (2.5), the identity $\nabla \cdot \boldsymbol{m} + \nabla \cdot \nabla\varphi = 0$ will not hold exactly at the discrete level. By setting the same physical parameters as in Figure 5.1, we assess the error of $\|\nabla \cdot (\boldsymbol{h} + \boldsymbol{m})\|$(note $\boldsymbol{h} = \nabla\varphi$) in Table 5.1, which shows that $\|\nabla \cdot (\boldsymbol{h} + \boldsymbol{m})\|$ approximates zero with first-order accuracy. Further, if we obtain $\boldsymbol{h} = P(\nabla\varphi)$, where $P : L^2(\Omega)^d \to \boldsymbol{N}_h$ is an L^2 projection, $\|\nabla \cdot (\boldsymbol{h} + \boldsymbol{m})\|$ approximates zero with almost third-order accuracy, as shown in Table 5.2.

TABLE 5.1
The error of $\|\nabla\cdot(\boldsymbol{h}+\boldsymbol{m})\|$ *with* $\delta t=\frac{1}{4}h$ *at* $t=1$ *of our scheme* (4.1)–(4.7).

h	$\frac{1}{4}$	$\frac{1}{8}$	$\frac{1}{16}$	$\frac{1}{32}$	$\frac{1}{64}$	$\frac{1}{128}$	$\frac{1}{256}$
$\|\nabla\cdot(\boldsymbol{h}+\boldsymbol{m})\|$	0.18308	0.045825	0.0085061	0.0020665	0.00064348	0.00021896	7.6359e-5
Order	–	1.99	2.43	2.04	1.68	1.55	1.51

TABLE 5.2
The error of $\|\nabla\cdot(\boldsymbol{h}+\boldsymbol{m})\|$ *with* $\delta t=\frac{1}{4}h$ *at* $t=1$ *of our scheme* (4.1)–(4.7) *by* L^2 *projection.*

h	$\frac{1}{4}$	$\frac{1}{8}$	$\frac{1}{16}$	$\frac{1}{32}$	$\frac{1}{64}$	$\frac{1}{128}$	$\frac{1}{256}$
$\|\nabla\cdot(\boldsymbol{h}+\boldsymbol{m})\|$	0.15054	0.031753	0.0043840	0.00057230	7.3544e-5	9.4267e-6	1.2223e-6
Order	–	2.24	2.85	2.93	2.96	2.96	2.94

5.2. Stability. In this subsection, we verify the stability of the proposed scheme (4.1)–(4.7). To better understand the stability of our scheme, we compare it with a second-order implicit-explicit decoupled-type scheme, described as follows:

(5.4)
$$
\begin{cases}
(\tilde{D}_t\boldsymbol{u}^{n+1},\boldsymbol{v})+\nu(\nabla\tilde{\boldsymbol{u}}^{n+1},\nabla\boldsymbol{v})+\nu_r(\nabla\times\tilde{\boldsymbol{u}}^{n+1},\nabla\times\boldsymbol{v})\\
\qquad\qquad +\nu_r(\nabla\cdot\tilde{\boldsymbol{u}}^{n+1},\nabla\cdot\boldsymbol{v})+((\boldsymbol{u}^*\cdot\nabla)\boldsymbol{u}^*,\boldsymbol{v})+(\nabla p^n,\boldsymbol{v})=2\nu_r(\boldsymbol{w}^*,\nabla\times\boldsymbol{v})\\
\qquad\qquad -\mu((\boldsymbol{v}\cdot\nabla)\boldsymbol{m}^*,\boldsymbol{h}^*)-\mu((\nabla\cdot\boldsymbol{v})\boldsymbol{m}^*,\boldsymbol{h}^*),\\
(\nabla p^{n+1},\nabla q)=-\dfrac{3}{2\delta t}(\nabla\cdot\tilde{\boldsymbol{u}}^{n+1},q)+(\nabla p^n,\nabla q),\\
\qquad \boldsymbol{u}^{n+1}=\tilde{\boldsymbol{u}}^{n+1}-\dfrac{2\delta t}{3}\nabla p^{n+1}+\dfrac{2\delta t}{3}\nabla p^n,\\
\zeta(D_t\boldsymbol{w}^{n+1},\boldsymbol{Z})+c_1(\nabla\boldsymbol{w}^{n+1},\nabla\boldsymbol{Z})+c_2(\nabla\cdot\boldsymbol{w}^{n+1},\nabla\cdot\boldsymbol{Z})+4\nu_r(\boldsymbol{w}^{n+1},\boldsymbol{Z})\\
\qquad\qquad +\zeta((\boldsymbol{u}^*\cdot\nabla)\boldsymbol{w}^*,\boldsymbol{Z})=2\nu_r(\nabla\times\boldsymbol{u}^*,\boldsymbol{Z})+\mu(\boldsymbol{m}^*\times\boldsymbol{h}^*,\boldsymbol{Z}),\\
(\nabla D_t\varphi^{n+1},\nabla\psi)+\dfrac{1}{\tau}(\nabla\varphi^{n+1},\nabla\psi)+\dfrac{\chi_0}{\tau}(\nabla\varphi^{n+1},\nabla\psi)-((\boldsymbol{u}^*\cdot\nabla)\boldsymbol{m}^*,\nabla\psi)\\
\qquad\qquad +(\boldsymbol{w}^*\times\boldsymbol{m}^*,\nabla\psi)=\dfrac{1}{\tau}(\boldsymbol{h}_a^{n+1},\nabla\psi)+(\boldsymbol{h}_b^{n+1},\nabla\psi),\\
(D_t\boldsymbol{m}^{n+1},\boldsymbol{n})+\dfrac{1}{\tau}(\boldsymbol{m}^{n+1},\boldsymbol{n})+((\boldsymbol{u}^*\cdot\nabla)\boldsymbol{m}^*,\boldsymbol{n})=(\boldsymbol{w}^*\times\boldsymbol{m}^*,\boldsymbol{n})+\dfrac{\chi_0}{\tau}(\boldsymbol{h}^{n+1},\boldsymbol{n}).
\end{cases}
$$

Within the above scheme, the discretization of all nonlinear terms is carried out explicitly, while the discretization of all linear terms is executed in an implicit manner. Though (5.4) has second-order convergence, as shown in Figure 5.3, it is well known that this type of implicit-explicit scheme is conditionally stable.

We set the computational domain as $\Omega=[0,1]^2$, the mesh size as $h=\frac{1}{64}$, and the applied magnetic field as $\boldsymbol{h}_a=\boldsymbol{0}$. The initial data read as

$$
\begin{cases}
\boldsymbol{u}_0=(x^2(x-1)^2y(y-1)(2y-1),-y^2(y-1)^2x(x-1)(2x-1)),\\
w_0=\sin(2\pi x)\sin(2\pi y),\quad \boldsymbol{m}_0=(\cos(2\pi y),\cos(2\pi x)).
\end{cases}
$$

We set the model parameters as $\chi_0=\zeta=\tau=1$ and vary ν,ν_r,c_1, and μ. We plot the evolution curves of the original energy in Figure 5.4, as defined in (2.8), using the scheme (5.4) with different time steps. We find that the scheme (5.4) blows up rapidly, even when the time step is as small as $\delta t=\frac{1}{20000}$ in some situations. For comparison, we plot the energy curves computed by our developed scheme with varying time steps. As shown in Figure 5.5, all the energy curves show a monotonic decrease, indicating that our scheme is energy stable.

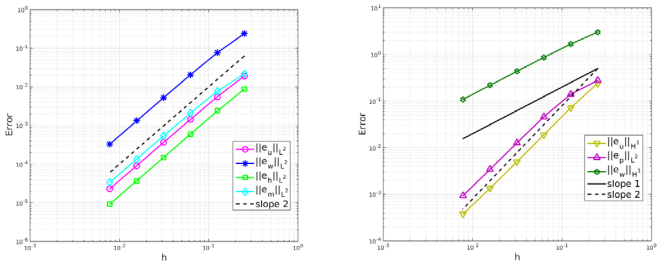

FIG. 5.3. *Numerical errors computed by the scheme* (5.4) *with* $\delta t = \frac{1}{2}h$ *and* $\nu = \nu_r = \mu = \zeta = c_1 = \chi_0 = 1, \tau = 0.1$ *using the analytical solution in subsection* 5.1.

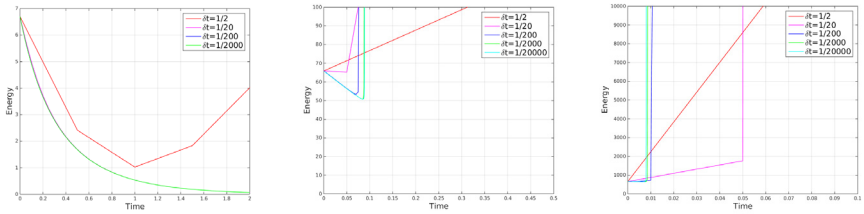

(a) ν=ν_r=c_1=0.1, μ=10. (b) ν=ν_r=c_1=0.01, μ=100. (c) ν=ν_r=c_1=0.001, μ=1000.

FIG. 5.4. *Energy curves computed by implicit-explicit scheme* (5.4)*, where model parameters* $\chi_0 = \zeta = \tau = 1$*, and* ν, ν_r, c_1*, and* μ *are varied.*

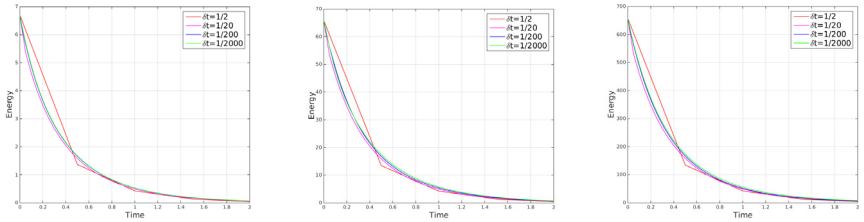

(a) ν=ν_r=c_1=0.1, μ=10. (b) ν=ν_r=c_1=0.01, μ=100. (c) ν=ν_r=c_1=0.001, μ=1000.

FIG. 5.5. *Energy curves computed by our scheme* (4.1)–(4.7) *where model parameters* $\chi_0 = \zeta = \tau = 1$*, and* ν, ν_r, c_1*, and* μ *are varied.*

Moreover, by increasing the model parameter ν_r, we aim to verify the effect of the stronger ***u*-*w*** linear coupling on the stability of the scheme. In Figures 5.6 and 5.7, for three different coupling parameters $\nu_r = 100$, 1000, 10000, we compare the energy curves computed by the scheme (5.4) and our scheme with various time steps. It is clear that when we use scheme (5.4), the energy exhibits a tendency to destabilize as the time step increases. In particular, when $\nu_r = 10000$, the energy profile computed by the scheme (5.4) blows up rapidly even when the time step is refined to $\frac{1}{20000}$. On the contrary, using the same model parameters, our proposed scheme consistently maintains unconditional stability over all time steps tested.

5.3. 2D/3D spin-up flow. The occurrence of spin-up flow was initially documented in 1967, demonstrating that a ferrofluid within a container rotates in a manner similar to a rigid body when subjected to a magnetic field that is delivered in a rotating form [18]. Several studies have investigated this issue using experiments and

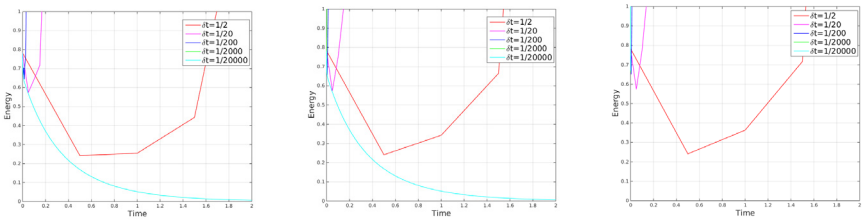

(a) $\nu_r = 100$ (b) $\nu_r = 1000$ (c) $\nu_r = 10000$

FIG. 5.6. *Energy curves computed by implicit-explicit scheme* (5.4) *for various* ν_r *and other physical parameters* $= 1$.

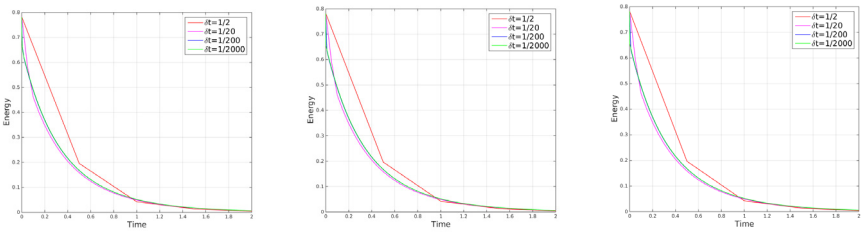

(a) $\nu_r = 100$ (b) $\nu_r = 1000$ (c) $\nu_r = 10000$

FIG. 5.7. *Energy curves computed by our scheme* (4.1)–(4.7) *for various* ν_r *and other physical parameters* $= 1$.

asymptotic analyses; see [6, 16, 24, 28, 35]. In this section, we simulate this phenomenon by employing the Rosensweig model and our developed numerical scheme for it.

5.3.1. 2D spin-up flow. We first simulate the spin-up flow behavior in 2D. We consider a ferrofluid container $\Omega = \{(x, y) \in \mathbb{R}^2 | x^2 + y^2 \leq \frac{1}{4}\}$ and set the physical parameters as

$$\nu = \nu_r = \mu = \zeta = c_1 = \chi_0 = 1.0, \ \tau = 1/10000, \ \delta t = 1/1000, \ h = 1/128. \tag{5.5}$$

We start from the case of applying a single rotary dipole, which is generated by using the formulation given in (5.1) with $s = 1$:

$$\boldsymbol{h}_a = \alpha \nabla \phi(\boldsymbol{x}), \tag{5.6}$$

where $\alpha = 1e6$, $\boldsymbol{d} = (-\cos((t-0.5)\pi), -\sin((t-0.5)\pi))$, $\boldsymbol{x}_s = (r\cos((t-0.5)\pi), r\sin((t-0.5)\pi))$ with $r = 100$. This dipole rotates around the center $(0, 0)$ with the direction $\boldsymbol{d}$ pointing toward the center, radius $r = 100$, and period 2 seconds; see the schematic setup shown in Figure 5.8(a). In Figure 5.8(b), we plot the computed velocity field at $t = 1s$, which demonstrates that the ferrofluid corotates with the applied magnetic field. The computed profiles of pressure, angular velocity, and magnetization at $t = 1s$ are also shown in Figure 5.8(c)–(e), respectively. The error of $\|\nabla \cdot (\boldsymbol{h} + \boldsymbol{m})\|$ with the time is also recorded in Figure 5.9, and we see it fluctuates periodically around 10^{-5}–10^{-4}. We set small diffusive coefficients $\nu = \nu_r = c_1 = 0.01$, and other parameters in (5.5) remain unchanged. Similar rotational flow also occurs; see Figure 5.10.

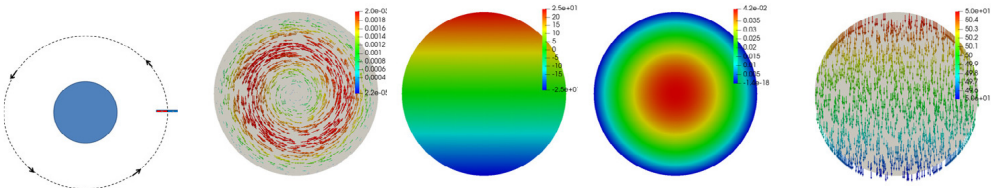

(a) Schematic setup. (b) Velocity. (c) Pressure. (d) Angular velocity. (e) Magnetization.

FIG. 5.8. *2D spin-up flow with single rotary dipole, where* (a) *is the schematic setup, and* (b)–(e) *are the computed velocity field, pressure, angular velocity, and magnetization at* $t = 1s$.

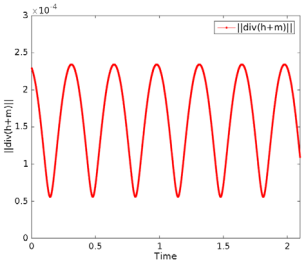

FIG. 5.9. *2D spin-up flow with single rotary dipole:* $\|\nabla \cdot (\boldsymbol{h} + \boldsymbol{m})\|$ *from* $t = 0$ *to* 2.1 *s.*

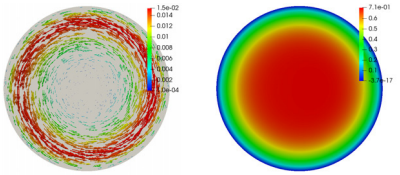

(a) Velocity. (b) Angular velocity.

FIG. 5.10. *2D spin-up flow with single rotary dipole for small diffusions* $\nu = \nu_r = c_1 = 0.01$, *where* (a) *is the velocity, and* (b) *is the angular velocity at* $t = 1s$.

Further, we continue to simulate the case of applying two rotary dipoles that is generated by

$$\boldsymbol{h}_a = \boldsymbol{h}_{a1} + \boldsymbol{h}_{a2}, \tag{5.7}$$

where $\boldsymbol{h}_{a1}$ is the same as (5.6), and $\boldsymbol{h}_{a2} = \boldsymbol{h}_{a1}(t+1)$. The schematic depiction of the experimental setup is presented in Figure 5.11(a), while Figure 5.11(b) displays the computed velocity field at $t = 1s$. We observe that the ferrofluid also corotates with the external magnetic field, but with a smaller amplitude. Figure 5.11(c)–(e) presents the computed pressure, angular velocity, and magnetization field at $t = 1s$, respectively.

5.3.2. 3D spin-up flow. In this example, we undertake the simulation of the 3D spin-up flow phenomenon, where the ferrofluids are enclosed in a cylinder container $\Omega = \{(x, y, z) \in \mathbb{R}^3 | [x^2 + y^2 \leq \frac{1}{4}] \times [0, \frac{1}{2}]\}$. The model physical parameters are the same as in the 2D case, and we set $\delta t = 1/10000$ and $h = 1/16$.

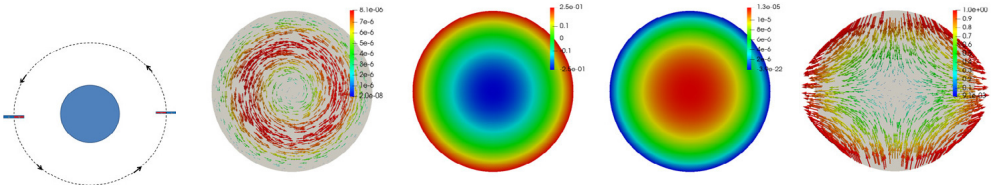

(a) Schematic setup. (b) Velocity. (c) Pressure. (d) Angular velocity. (e) Magnetization.

FIG. 5.11. *2D spin-up flow with two rotary dipoles, where* (a) *is the schematic setup, and* (b)-(e) *are the computed velocity field, pressure, angular velocity, and magnetization at* $t = 1s$.

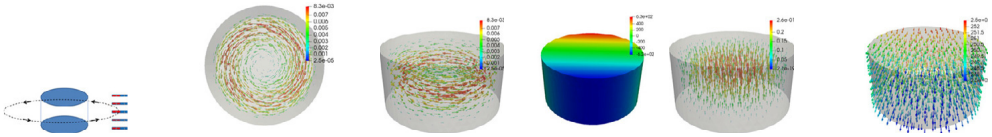

(a) Schematic setup. (b) Top view velocity. (c) Side view velocity. (d) Pressure. (e) Angular velocity. (f) Magnetization.

FIG. 5.12. *3D spin-up flow with one group of five rotary dipoles, where* (a) *is the schematic setup, and* (b)–(f) *are the computed velocity field (top view and side view), pressure, angular velocity, and magnetization at* $t = 1s$.

First, we simulate an applied magnetic field configuration comprising a group of five rotary dipoles that are generated by

$$\boldsymbol{h}_a = \sum_{s=1}^{5} \alpha_s \nabla \phi_s(\boldsymbol{x}), \tag{5.8}$$

where $\alpha_s = 1e6$, $\boldsymbol{d} = (-\cos((t-0.5)\pi), -\sin((t-0.5)\pi), 0.0)$, $\boldsymbol{x}_s = (r\cos((t-0.5)\pi), r\sin((t-0.5)\pi), pz_s)$ with $r = 100$, $pz_s = \frac{s-1}{8}$, $s = 1, 2, \ldots, 5$. Figure 5.12 displays the schematic setup, the computed velocity field with two different viewing perspectives, and the pressure, angular velocity, and magnetization at $t = 1s$. It is evident from the results that the ferrofluid exhibits rotation in synchronization with the applied rotational magnetic field, consistent with our observations in the 2D simulation.

Second, we simulate a configuration comprising two groups of ten rotary dipoles in total that are defined as

$$\boldsymbol{h}_a = \boldsymbol{h}_{a1} + \boldsymbol{h}_{a2}, \tag{5.9}$$

where $\boldsymbol{h}_{a1}$ is the same as (5.8), and $\boldsymbol{h}_{a2}(t) = \boldsymbol{h}_{a1}(t+1)$. We adopt $\delta t = 1/1000, h = 1/32$. The schematic setup and the computed profiles, including the velocity field with two different views, pressure, angular velocity, and magnetization at $t = 2s$, are shown in Figure 5.13. As observed in the 2D simulations, the ferrofluid flows in alignment with the rotational magnetic field but with lower magnitude than the one-group-of-five-dipoles case.

5.4. 2D/3D annulus flow. The behavior of the ferrofluid within an annulus domain differs significantly from that of the spin-up flow. Experiments and analyses have revealed that with one applied dipole, the ferrofluid rotates in the opposite direction with respect to the magnetic field close to the inner cylinder, and corotates with respect to the magnetic field close to the outer cylinder. However, with an applied magnetic field using two dipoles, the ferrofluid corotates with the magnetic

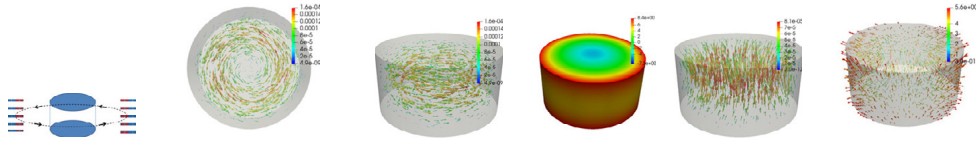

(a) Schematic setup. (b) Top view velocity. (c) Side view velocity. (d) Pressure. (e) Angular velocity. (f) Magnetization.

FIG. 5.13. *3D spin-up flow with two groups of ten dipoles, where* (a) *is the schematic setup, and* (b)–(f) *are the computed velocity field (top view and side view), pressure, angular velocity, and magnetization at* $t = 2s$.

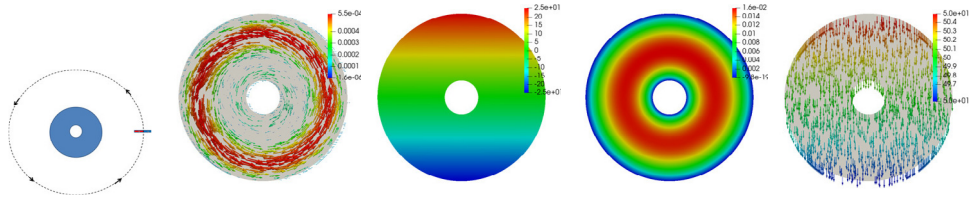

(a) Schematic setup. (b) Velocity. (c) Pressure. (d) Angular velocity. (e) Magnetization.

FIG. 5.14. *2D annulus flow with single rotary dipole, where* (a) *is the schematic setup, and* (b)–(e) *are the computed velocity field, pressure, angular velocity, and magnetization at* $t = 1s$.

field in the annulus region; cf. [5, 8]. In this section, we use the Rosensweig model and our developed scheme to simulate the 2D/3D annulus ferrofluid flows.

5.4.1. 2D annulus flow. We start with the one dipole case in 2D, where the dipole is defined as in (5.6). The computational domain is set as $\Omega = \{(x, y) \in \mathbb{R}^2 | \frac{1}{100} \leq x^2 + y^2 \leq \frac{1}{4}\}$, and the model parameters are still set as (5.5). The schematic setup and the computed profiles of the velocity, pressure, angular velocity, and magnetization at $t = 1s$ are shown in Figure 5.14. The velocity field shown in Figure 5.14(b) demonstrates that the ferrofluid exhibits counter-rotational behavior with respect to the magnetic field in proximity to the inner cylinder, whereas it corotates with the magnetic field in the remaining region of the container.

We continue to investigate the annulus flows under two dipoles that are defined as in (5.7). The schematic setup and the computed results at $t = 1s$ are shown in Figure 5.15. As depicted in Figure 5.15(b), it is clear that the fluid flows congruently with the rotational dipoles, a behavior that significantly contrasts with the scenario shown in Figure 5.14(b) when a single dipole is employed.

5.4.2. 3D annulus flow. We further carry out the 3D annulus ferrofluid flow simulation, where the physical model parameters are set as in (5.5), and the computational domain is set as $\Omega = \{(x, y, z) \in \mathbb{R}^3 \ |[\frac{1}{100} \leq x^2 + y^2 \leq \frac{1}{4}] \times [0, \frac{1}{2}]\}$.

We conduct a comparison between two simulations: one involving a group of five rotary dipoles, defined as in (5.8), and the other employing two groups of ten rotary dipoles, defined as in (5.9). These simulations utilize different spatial-temporal mesh sizes: $(h = 1/20, \delta t = 1/10000)$ for the former, and $(h = 1/64, \delta t = 1/10000)$ for the latter. Schematic setups and computed profiles of velocity, pressure, angular velocity, and magnetization for each case at different time points ($t = 0.5s$ for the first simulation and $t = 2s$ for the second simulation) of these two simulations are shown in Figure 5.16 and Figure 5.17, respectively. It can be seen that the 3D results are consistent with the 2D cases; namely, for the former case (one group of five rotary dipoles), the ferrofluid flows in counter-rotation with the applied magnetic

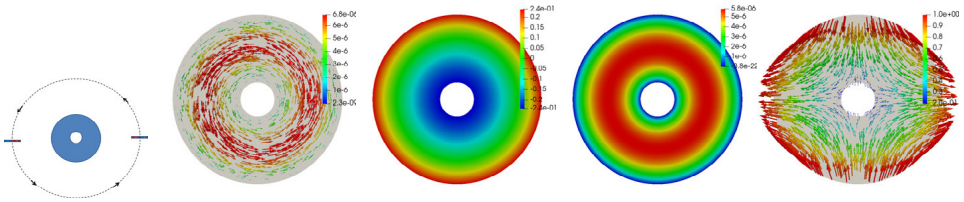

(a) Schematic setup. (b) Velocity. (c) Pressure. (d) Angular velocity. (e) Magnetization.

FIG. 5.15. *2D annulus flow with two rotary dipoles, where* (a) *is the schematic setup, and* (b)–(e) *are the computed velocity field, pressure, angular velocity, and magnetization at* $t = 1s$.

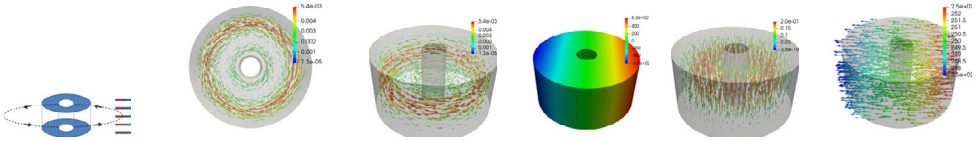

(a) Schematic setup. (b) Top view velocity. (c) Side view velocity (d) Pressure. (e) Angular velocity. (f) Magnetization.

FIG. 5.16. *3D annulus flow with one group of five rotary dipoles, where* (a) *is the schematic setup, and* (b)–(f) *are the computed velocity field (top view and side view), pressure, angular velocity, and magnetization at* $t = 0.5s$.

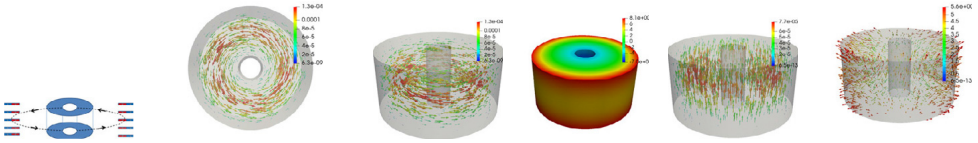

(a) Schematic setup. (b) Top view velocity (c) Side view velocity (d) Pressure. (e) Angular velocity. (f) Magnetization.

FIG. 5.17. *3D annulus flow with two groups of ten rotary dipoles, where* (a) *is the schematic setup, and* (b)-(f) *are the computed velocity field (top view and side view), pressure, angular velocity, and magnetization at* $t = 2s$.

field near the inner cylinder and in corotation with the magnetic field close to the outer cylinder; nevertheless, for the latter circumstance (two groups of ten rotary dipoles), the ferrofluid corotates with the external magnetic dipoles.

6. Concluding remarks. The Rosensweig FHD system is a highly sophisticated, coupled, and nonlinear multiphysics field model with a saddle-point structure. To develop an efficient energy-stable algorithm for this system, numerous numerical challenges, particularly those related to linear and nonlinear couplings, need to be appropriately addressed. This paper leverages various effective numerical techniques, such as the ZEC decoupling method and the projection method. In particular, a novel approach for solving the linear coupling between variables $\boldsymbol{u}$ and $\boldsymbol{w}$, utilizing an auxiliary variable and its associated ODE with a distinctive structure, is introduced, which can also be regarded as a generalized framework-type method applicable to systems with similar linear couplings. The numerical scheme proposed in this paper represents a novel methodology for the Rosensweig model, noteworthy for its integration of four essential properties: linearity, full decoupling, second-order accuracy, and unconditional energy stability. This efficient scheme is also very easy to implement by solving only a few independent linear elliptic/parabolic problems with constant coefficients. Applying this scheme to the Rosensweig model, we conduct benchmark

numerical experiments on ferrofluid rotational flow problems, focusing on 2D and 3D spin-up and annulus flows, and we confirm that the computed numerical simulations are in good agreement with both experimental and analytical results.

REFERENCES

[1] Y. Amirat and K. Hamdache, *Strong solutions to the equations of a ferrofluid flow model*, J. Math. Anal. Appl., 353 (2009), pp. 271–294, https://doi.org/10.1016/j.jmaa.2008.11.084.

[2] Y. Amirat, K. Hamdache, and F. Murat, *Global weak solutions to equations of motion for magnetic fluids*, J. Math. Fluid Mech., 10 (2008), pp. 326–351, https://doi.org/10.1007/s00021-006-0234-6.

[3] L. Arias, J. Pessan, A. Vieira, T. Lima, A. Delbem, and D. Monteiro, *Iron oxide nanoparticles for biomedical applications: A perspective on synthesis, drugs, antimicrobial activity, and toxicity*, Antibiotics, 7 (2018), 46, https://doi.org/10.3390/antibiotics7020046.

[4] S. C. Brenner and L. R. Scott, *The Mathematical Theory of Finite Element Methods*, Vol. 3, Springer, 2008.

[5] A. Chaves, I. Diaz, and C. Rinaldi, *Flow of ferrofluid in an annular gap in a rotating magnetic field*, Phys. Fluids, 22 (2010), https://doi.org/10.1063/1.3483598.

[6] A. Chaves, M. Zahn, and C. Rinaldi, *Spin-up flow of ferrofluids: Asymptotic theory and experimental measurements*, Phys. Fluids, 20 (2008), https://doi.org/10.1063/1.2907221.

[7] Y. Chen, A. Kolhatkar, O. Zenasni, S. Xu, and T. Lee, *Biosensing using magnetic particle detection techniques*, Sensors, 17 (2017), 2300, https://doi.org/10.3390/s17102300.

[8] I. Torres-Díaz and C. Rinaldi, *Ferrofluid flow in the annular gap of a multipole rotating magnetic field*, Phys. Fluids, 23 (2011), 082001, https://doi.org/10.1063/1.3611027.

[9] Y. Ding and F. Lin, *Semiclassical states of Hamiltonian system of Schrödinger equations with subcritical and critical nonlinearities*, J. Partial Differential Equations, 19 (2006), pp. 232–255, http://global-sci.org/intro/article_detail/jpde/5330.html.

[10] V. Girault and P. Raviart, *Finite Element Method for Navier-Stokes Equations: Theory and Algorithms*, Springer-Verlag, Berlin, Heidelberg, 1987.

[11] J. L. Guermond, P. Minev, and J. Shen, *An overview of projection methods for incompressible flows*, Comput. Methods Appl. Mech. Engrg., 195 (2006), pp. 6011–6045, https://doi.org/10.1016/j.cma.2005.10.010.

[12] K. Hayashi, W. Sakamoto, and T. Yogo, *Drug delivery: Smart ferrofluid with quick gel transformation in tumors for mri-guided local magnetic thermochemotherapy*, Adv. Funct. Mater., 26 (2016), pp. 1852–1852, https://doi.org/10.1002/adfm.201670071.

[13] J. Jackson, *Classical Electrodynamics*, John Wiley & Sons, 2021.

[14] D. Jamon, F. Donatini, A. Siblini, F. Royer, R. Perzynski, V. Cabuil, and S. Neveu, *Experimental investigation on the magneto-optic effects of ferrofluids via dynamic measurements*, J. Magn. Magn. Mater., 321 (2009), pp. 1148–1154, https://doi.org/10.1016/j.jmmm.2008.10.038.

[15] M. Kole and S. Khandekar, *Engineering applications of ferrofluids: A review*, J. Magn. Magn. Mater., 537 (2021), 168222, https://doi.org/10.1016/j.jmmm.2021.168222.

[16] A. V. Lebedev and A. F. Pschenichnikov, *Rotational effect: The influence of free or solid moving boundaries*, J. Magn. Magn. Mater., 122 (1993), pp. 227–230, https://doi.org/10.1016/0304-8853(93)91080-Q.

[17] M. Maier, J. N. Shadid, and I. Tomas, *Structure-preserving finite-element schemes for the Euler-Poisson equations*, Commun. Comput. Phys., 33 (2023), pp. 647–691, https://doi.org/10.4208/cicp.OA-2022-0205.

[18] R. Moskowitz and R. E. Rosensweig, *Nonmechanical torque-driven flow of a ferromagnetic fluid by an electromagnetic field*, Appl. Phys. Lett., 11 (1967), pp. 301–303, https://doi.org/10.1063/1.1754952.

[19] R. H. Nochetto, A. J. Salgado, and I. Tomas, *The micropolar navier–stokes equations: A priori error analysis*, Math. Models Methods Appl. Sci., 24 (2014), pp. 1237–1264, https://doi.org/10.1142/S0218202514500018.

[20] R. H. Nochetto, A. J. Salgado, and I. Tomas, *A diffuse interface model for two-phase ferrofluid flows*, Comput. Methods Appl. Mech. Engrg., 309 (2016), pp. 497–531, https://doi.org/10.1016/j.cma.2016.06.011.

[21] R. H. Nochetto, A. J. Salgado, and I. Tomas, *The equations of ferrohydrodynamics: Modeling and numerical methods*, Math. Models Methods Appl. Sci., 26 (2016), pp. 2393–2449, https://doi.org/10.1142/S0218202516500573.

[22] R. H. Nochetto, K. Trivisa, and F. Weber, *On the dynamics of ferrofluids: Global weak solutions to the Rosensweig system and rigorous convergence to equilibrium*, SIAM J. Math. Anal., 51 (2019), pp. 4245–4286, https://doi.org/10.1137/18M1224957.

[23] M. Pinho, J.-M. Génevaux, N. Dauchez, B. Brouard, P. Collas, and H. Mézière, *Damping induced by ferrofluid seals in ironless loudspeaker*, J. Magn. Magn. Mater., 356 (2014), pp. 125–130, https://doi.org/10.1016/j.jmmm.2013.12.047.

[24] A. F. Pshenichnikov, A. V. Lebedev, and M. I. Shliomis, *On the rotational effect in nonuniform magnetic fluids*, Magnetohydrodynamics, 36 (2000), pp. 275–281, http://doi.org/10.22364/mhd.

[25] I. Raouf, P. Gas, and H. Kim, *Numerical investigation of ferrofluid preparation during in-vitro culture of cancer therapy for magnetic nanoparticle hyperthermia*, Sensors, 21 (2021), 5545, https://doi.org/10.3390/s21165545.

[26] R. E. Rosensweig, *Ferrohydrodynamics*, Cambridge University Press, Cambridge, UK, 1985.

[27] R. E. Rosensweig, *Magnetic fluids*, Ann. Rev. Fluid Mech., 19 (1987), pp. 437–461, https://doi.org/10.1146/annurev.fl.19.010187.002253.

[28] R. E. Rosensweig, J. Popplewell, and R. J. Johnston, *Magnetic fluid motion in rotating field*, J. Magn. Magn. Mater., 85 (1990), pp. 171–180, https://doi.org/10.1016/0304-8853(90)90046-S.

[29] A. J. Salgado, *Convergence analysis of fractional time-stepping techniques for incompressible fluids with microstructure*, J. Sci. Comput., 64 (2015), pp. 216–233, https://doi.org/10.1007/s10915-014-9926-x.

[30] S. Scrobogna, *On the global well-posedness of a class of* $2D$ *solutions for the Rosensweig system of ferrofluids*, J. Differential Equations, 266 (2019), pp. 2718–2761, 10.1016/j.jde.2018.08.043.

[31] N. Shabani, A. Javadi, H. Jafarizadeh-Malmiri, H. Mirzaie, and J. Sadeghi, *Potential application of iron oxide nanoparticles synthesized by co-precipitation technology as a coagulant for water treatment in settling tanks*, Mining Metallurgy Exploration, 38 (2021), pp. 269–276, https://doi.org/10.1007/s42461-020-00338-y.

[32] J. Shen, *On error estimates of projection methods for the Navier-Stokes equations: Second-order schemes*, Math. Comp., 65 (1996), pp. 1039–1065, https://doi.org/10.1090/S0025-5718-96-00750-8.

[33] M. I. Shliomis, *Effective viscosity of magnetic suspensions*, Sov. Phys. JETP, 34 (1972), pp. 1291–1294.

[34] M. I. Shliomis, *Ferrohydrodynamics: Retrospective and issues*, in Ferrofluids, S. Odenbach, ed., Lect. Notes Phys. 594, Springer, Berlin, 2002, pp. 85–111, https://doi.org/10.1007/3-540-45646-5_5.

[35] M. I. Shliomis, *How a rotating magnetic field causes ferrofluid to rotate*, Phys. Rev. Fluids, 6 (2021), 043701, https://doi.org/10.1103/PhysRevFluids.6.043701.

[36] S. Slayi, T. El Arwadi, and S. Dib, *Stabilized Gauge Uzawa scheme for an incompressible micropolar fluid flow*, Appl. Numer. Math., 167 (2021), pp. 45–72, https://doi.org/10.1016/j.apnum.2021.04.003.

[37] Z. Tan and Y. Wang, *Global analysis for strong solutions to the equations of a ferrofluid flow model*, J. Math. Anal. Appl., 364 (2010), pp. 424–436, https://doi.org/10.1016/j.jmaa.2009.10.032.

[38] R. Temam, *Infinite-Dimensional Dynamical Systems in Mechanics and Physics*, Appl. Math. Sci. 68, Springer-Verlag, New York, 1997.

[39] Y. Wang and Z. Tan, *Global existence and asymptotic analysis of weak solutions to the equations of ferrohydrodynamics*, Nonlinear Anal. Real World Appl., 11 (2010), pp. 4254–4268, https://doi.org/10.1016/j.nonrwa.2010.05.012.

[40] Y. Wu and X. Xie, *Energy-stable mixed finite element methods for a ferrofluid flow model*, Commun. Nonlinear Sci. Numer. Simul., 125 (2023), 107330, https://doi.org/10.1016/j.cnsns.2023.107330.

[41] X. Yang, *A novel fully-decoupled, second-order and energy stable numerical scheme of the conserved Allen-Cahn type flow-coupled binary surfactant model*, Comput. Methods Appl. Mech. Engrg., 373 (2021), 113502, https://doi.org/10.1016/j.cma.2020.113502.

[42] X. Yang, *A novel fully-decoupled, second-order time-accurate, unconditionally energy stable scheme for a flow-coupled volume-conserved phase-field elastic bending energy model*, J. Comput. Phys., 432 (2021), 110015, https://doi.org/10.1016/j.jcp.2020.110015.

[43] X. Yang, *On a novel fully decoupled, second-order accurate energy stable numerical scheme for a binary fluid-surfactant phase-field model*, SIAM J. Sci. Comput., 43 (2021), pp. B479–B507, https://doi.org/10.1137/20M1336734.

[44] J. Yao, D. Li, X. Chen, C. Huang, and D. Xu, *Damping performance of a novel ferrofluid dynamic vibration absorber*, J. Fluid. Struct., 90 (2019), pp. 190–204, https://doi.org/10.1016/j.jfluidstructs.2019.06.009.

[45] G. D. Zhang, X. He, and X. Yang, *Decoupled, linear, and unconditionally energy stable fully discrete finite element numerical scheme for a two-phase ferrohydrodynamics model*, SIAM J. Sci. Comput., 43 (2021), pp. B167–B193, https://doi.org/10.1137/19M1288280.

[46] G. D. Zhang, X. He, and X. Yang, *A fully decoupled linearized finite element method with second-order temporal accuracy and unconditional energy stability for incompressible mhd equations*, J. Comput. Phys., 448 (2022), 110752, https://doi.org/10.1016/j.jcp.2021.110752.

[47] G. D. Zhang, X. He, and X. Yang, *Reformulated weak formulation and efficient fully discrete finite element method for a two-phase ferrohydrodynamics shliomis model*, SIAM J. Sci. Comput., 45 (2023), pp. B253–B282, https://doi.org/10.1137/22M1499376.

[48] X. Zhang and X. Long, *Unconditional stability and error analysis of an euler imex-sav scheme for the micropolar navier-stokes equations*, Appl. Numer. Math., 192 (2023), pp. 214–240, https://doi.org/10.1016/j.apnum.2023.05.027.